Precise Spatial Tuning of Visually Driven Alpha Oscillations in Human Visual Cortex

Kenichi Yuasa[1], Iris I.A. Groen[1,2], Giovanni Piantoni[3], Stephanie Montenegro[4], Adeen Flinker[4], Sasha Devore[4], Orrin Devinsky[4], Werner Doyle[4], Patricia Dugan[4], Daniel Friedman[4], Nick Ramsey[3], Natalia Petridou[3], Jonathan Winawer[1]

[1]Department of Psychology, New York University, New York, NY, USA
[2]Video & Image Sense Lab, Informatics Institute, University of Amsterdam, Amsterdam, The Netherlands
[3]University Medical Center Utrecht, Utrecht, The Netherlands
[4]New York University School of Medicine, New York, NY, USA

Abstract

Neuronal oscillations at about 10 Hz, called alpha oscillations, are often thought to arise from synchronous activity across occipital cortex, reflecting general cognitive states such as arousal and alertness. However, there is also evidence that modulation of alpha oscillations in visual cortex can be spatially specific. Here, we used intracranial electrodes in human patients to measure alpha oscillations in response to visual stimuli whose location varied systematically across the visual field. We separated the alpha oscillatory power from broadband power changes. The variation in alpha oscillatory power with stimulus position was then fit by a population receptive field (pRF) model. We find that the alpha pRFs have similar center locations to pRFs estimated from broadband power (70–180 Hz) but are several times larger. The results demonstrate that alpha suppression in human visual cortex can be precisely tuned. Finally, we show how the pattern of alpha responses can explain several features of exogenous visual attention.

Significance Statement: The alpha oscillation is the largest electrical signal generated by the human brain. An important question in systems neuroscience is the degree to which this oscillation reflects system-wide states and behaviors such as arousal, alertness, and attention, versus much more specific functions in the routing and processing of information. We examined alpha oscillations at high spatial precision in human patients with intracranial electrodes implanted over visual cortex. We discovered a surprisingly high spatial specificity of visually driven alpha oscillations, which we quantified with receptive field models. We further use our discoveries about properties of the alpha response to show a link between these oscillations and the spread of visual attention.

Keywords: visual cortex, alpha oscillations, exogenous attention, electrocorticography (ECoG), intracranial electroencephalography (iEEG), computational models, population receptive fields (pRF)

Grant support: NIH R01 MH111417 (Petridou, Winawer, Ramsey, Devinsky); JSPS Overseas Research Fellowship (Yuasa)

The content is solely the responsibility of the authors and does not necessarily represent the official views of the National Institutes of Health

1. INTRODUCTION

Hans Berger first measured electrical oscillations at 10 Hz from the human brain using EEG (Berger, 1929). Shortly thereafter, Adrian and Matthews (1934) confirmed that when a participant closes their eyes or views a uniform field, the oscillatory power increases. They described the alpha oscillation as "show[ing] the negative rather than the positive side of cerebral activity; it shows what happens in an area of cortex which has nothing to do, and it disappears as soon as the area resumes its normal work". Consistent with this interpretation, alpha oscillatory power is reduced by arousal (Barry, Clarke, Johnstone, Magee, & Rushby, 2007) and alertness (Matousek & Petersen, 1983). The negative association between alpha oscillations and cerebral activity can also be more specific. For example, when attending a location to the left or right of fixation, the occipital alpha power measured by EEG decreases contralaterally and increases ipsilaterally (Kelly, Lalor, Reilly, & Foxe, 2006; Sauseng et al., 2005; Worden, Foxe, Wang, & Simpson, 2000), opposite to the fMRI response (reviewed by Carrasco, 2011; Somers, Dale, Seiffert, & Tootell, 1999). The reduction in alpha power can also be specific to cortical locations representing narrow angular wedges in the visual field, as measured by both EEG and MEG (Foster, Sutterer, Serences, Vogel, & Awh, 2017; Popov, Gips, Kastner, & Jensen, 2019; Rihs, Michel, & Thut, 2007; Samaha, Sprague, & Postle, 2016). The common finding across these studies is that the strength of the alpha rhythm is lower in the part of cortex that is more active.

It is therefore surprising that studies examining the spatial tuning of alpha oscillations with invasive methods have tended to find a positive association between alpha oscillations and cortical activity. Specifically, two studies in macaque measured spatial receptive fields using power in the alpha band as a dependent measure, and found that for most recording sites, alpha power increased rather than decreased when a stimulus was in the receptive field (Klink, Chen, Vanduffel, & Roelfsema, 2021; Takaura, Tsuchiya, & Fujii, 2016). A positive association has also been found in human intracortical studies, reporting power increases in the alpha band when stimuli were in or near electrode receptive fields (Harvey et al., 2013; Luo et al., 2023).

Why do the intracranial studies on spatial tuning find increases in alpha oscillations, whereas the MEG and EEG studies find decreases? One difference is that cortical engagement was stimulus-driven in the intracranial studies and task-driven (spatial attention) in the MEG and EEG studies. We speculate that both visual stimulation and visual attention tend to decrease alpha oscillations, but that visual stimulation masks the alpha decrease with a simultaneous increase in broadband neural responses. Broadband spectral power increases are observed in many intracranial studies in association with increased neural activity (Crone, Miglioretti, Gordon, & Lesser, 1998; Hermes, Nguyen, & Winawer, 2017; Miller, Sorensen, Ojemann, & den Nijs, 2009; Winawer et al., 2013) and likely have a distinct biological cause from oscillations (Hermes et al., 2017; Ray & Maunsell, 2011). Because a visual stimulus can cause a simultaneous increase in broadband power and decrease in alpha oscillatory power, a power change at the alpha frequency is ambiguous. Separating responses by frequency band does not resolve the ambiguity because broadband power changes can extend to low frequencies, including the alpha band (Winawer et al., 2013).

Here, we examined how alpha oscillations are modulated in human visual cortex by visual stimulation using electrocorticographic (ECoG) recordings in 9 participants. We addressed two main questions: First, are alpha oscillations increased or decreased by visual stimulation? Second, what is the spatial specificity of the modulation of alpha oscillations? To answer these questions, we used a modeling approach to separate the alpha oscillation from non-oscillatory (broadband) responses. We then used population receptive field (pRF) modeling to quantify the spatial tuning of separate components of the ECoG signal, corresponding to alpha oscillations and broadband responses.

By separating the ECoG voltage time course into distinct components, we find that the broadband signal is increased and the alpha oscillation is decreased by visual stimulation. We also find that the broadband pRFs

and alpha pRFs have similar locations (center positions) but differ in size. Together, the results suggest that the alpha oscillation in human visual cortex is spatially tuned and negatively modulated by visual input. In the Discussion, we consider how the spatially tuned reduction in the alpha oscillation may contribute to visual function, showing a surprisingly tight link between the spatial profiles of the stimulus-driven alpha oscillation on the one hand, and the behavioral effects of spatial attention on the other hand. Finally, we show how the former may give rise to the latter.

2. RESULTS

2.1 TWO SIGNATURES OF VISUAL RESPONSES MEASURED WITH ELECTROCORTICOGRAPHY

Visual stimulation causes a variety of temporal response patterns measured in visual cortex. In addition to the evoked potential, which is a characteristic change in voltage time-locked to the stimulus onset, there are also spectral perturbations (Makeig, 1993). The largest such perturbation is the alpha oscillation. Typically, when the eyes are closed or when the participant views a blank screen (no stimulus contrast) the field potential measured from visual cortex oscillates at about 8 to 13 Hz (Berger, 1929). Opening the eyes or viewing a stimulus reduces this oscillation. In addition to these spectral perturbations, there is also a broadband response, an increase in power across a wide frequency range following stimulus onset (Manning, Jacobs, Fried, & Kahana, 2009; Miller, Sorensen, et al., 2009). Both the broadband increase and alpha suppression can be elicited by the same stimulus and measured from the same electrode. In the example shown in **Figure 1**, stimulus onset caused a broadband increase in power spanning the full range plotted, from 1 Hz to 150 Hz, and it eliminated the peak in the alpha range. The two types of response cannot be separated by simply applying filters with different temporal frequency ranges because the signals overlap in the low frequency range (6 to 22 Hz in **Figure 1f**).

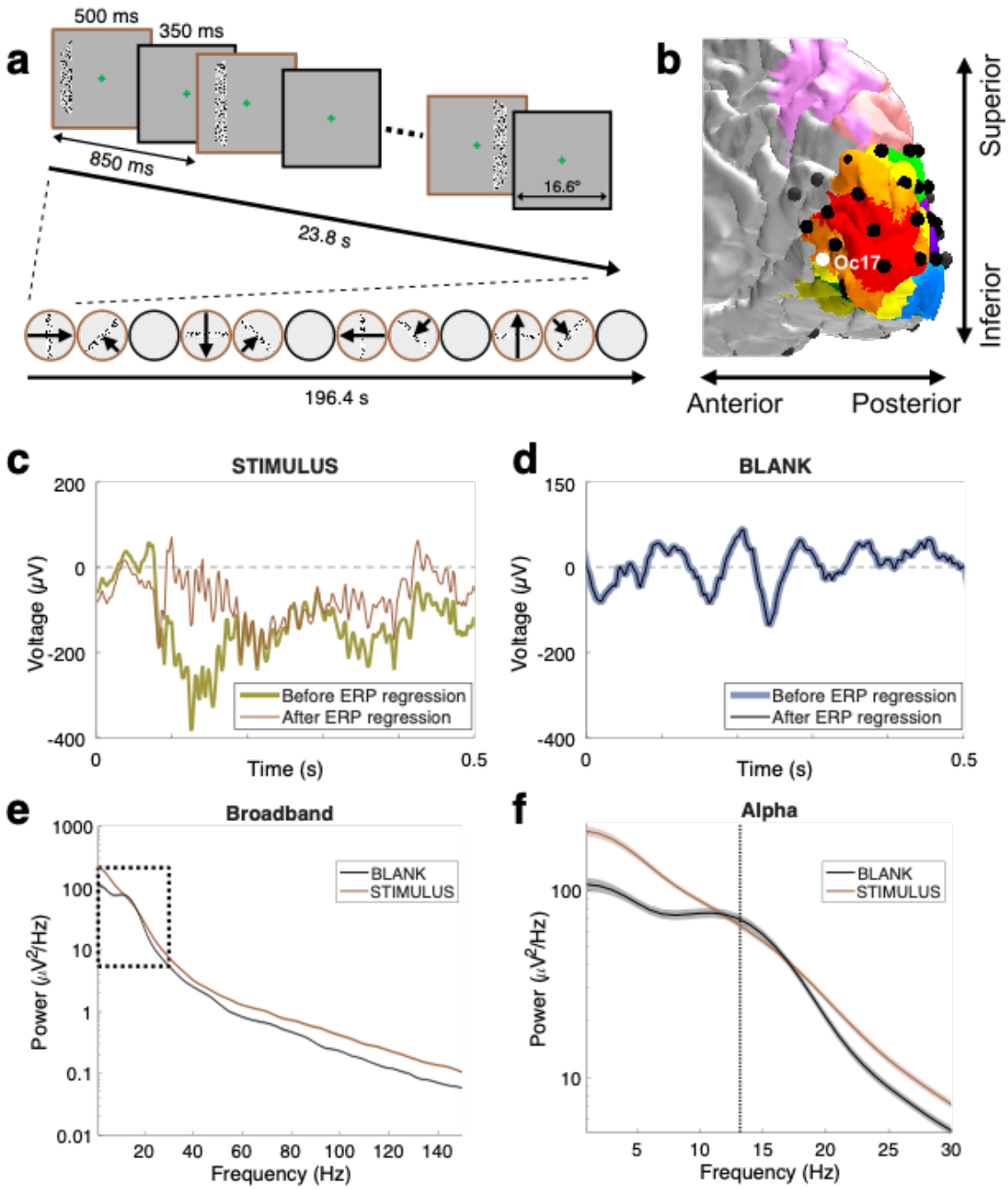

Figure 1. Two signatures of visual responses measured with ECoG. (**a**) Mapping stimuli. Three examples of the bar stimuli and one image of the blank stimulus during the mapping experiment (brown and black outlines, respectively). The contrast within the bar is increased here for visibility. (**b**) A close-up view of the right occipital cortex of Patient 2. The surface colors show several visual field maps derived from an atlas, with V1 in red, V2 in orange, and V3 in yellow. Black circles indicate ECoG electrode locations. (See **Supplementary Figure 1-1** for all patients) (**c**) The voltage signal during a single trial with a stimulus present for electrode Oc17. The thick and thin lines are voltages before and after regressing out the ERP, respectively. Note the sharp high frequency oscillations in both traces, and the lack of a clear alpha oscillation. (**d**) Same but for a single blank trial. Here, the two signals are nearly identical since there is no ERP during a blank trial. Note the strong alpha oscillation. (See **Supplementary Figure 1-2** for the effect of ERP removal processing in pRF estimation.) (**e**) The power spectral density (PSD) was computed based on the regressed signal, averaged across all blank trials (black) or all stimulus trials (brown). The stimulus causes a broadband power increase, spanning frequencies from 1 Hz to 150 Hz. The dotted black rectangle indicates the frequency range shown in zoom in panel **f**. (**f**) During the blank, but not during visual stimulation, there is a peak in the spectrum at around 13 Hz (alpha oscillation, dashed vertical line). Shading represents the standard error across trials (320 trials for stimulus, 128 trials for blank). See *makeFigure1.m*.

2.2 Separating the alpha oscillation from broadband power

Because stimulus onset tends to cause an increase in broadband power and a decrease in the alpha oscillation, it is possible for the two effects to cancel at some frequencies. In the example shown in **Figure 1**, the power at the peak of the alpha oscillation (~13 Hz, black dashed line) is nearly the same during stimulus and blank. It would be incorrect, however, to infer that the alpha oscillation was unaffected by the stimulus. Rather, the decrease in the alpha oscillation and the increase in broadband power were about equal in magnitude. Depending on the relative size of these two spectral responses, the power at the alpha frequency can increase, decrease, or not change. We illustrate these possibilities with three nearby electrodes from one patient (**Figure 2**). For all three electrodes as shown in the left panels, there is a peak in the alpha range during blanks (black lines) but not during visual stimulation (brown lines). Due to the interaction with the broadband response, the power at the peak alpha frequency for stimulus relative to blank increased slightly for one electrode (Oc18), decreased slightly for a second electrode (Oc17), and decreased more substantially for a third electrode (Oc25). By adjusting the baseline to account for the broadband response as shown in the right panels, it is clear that the stimulus caused the alpha oscillation to decrease for all three electrodes. For these reasons, simply comparing the spectral power at the alpha frequency between two experimental conditions is not a good indicator of the strength of the alpha rhythm. To separate the alpha oscillation from the broadband change, we applied a baseline correction using a model-based approach.

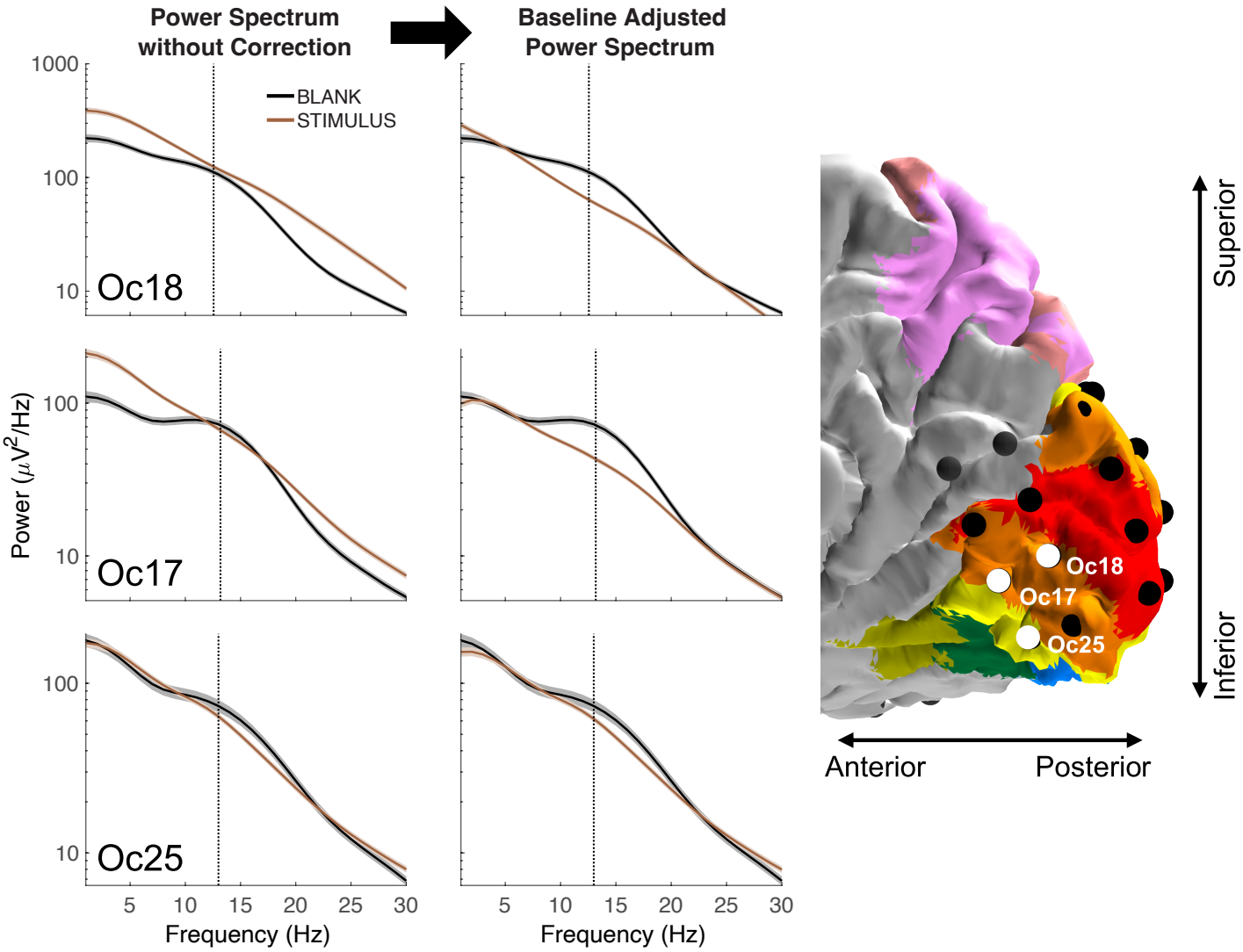

Figure 2. Interaction between the alpha rhythm and broadband power. (Left column) PSDs from 3 electrodes in Patient 2 without baseline correction show that the stimulus-related alpha power can slightly increase (Oc18), slightly decrease (Oc17) or substantially decrease (Oc25) relative to a blank stimulus. (Right column) After correcting for the broadband shift, it is clear that for all three electrodes, the alpha oscillation is suppressed by visual stimulation. The dashed vertical lines indicate the alpha peak frequency. Shading represents the standard error across trials (320 trials for stimulus, 128 trials for blank). See Methods and *makeFigure2.m*.

2.3 ALPHA RESPONSES ARE ACCURATELY PREDICTED BY A POPULATION RECEPTIVE FIELD MODEL

By estimating the alpha oscillatory power change from the low-frequency decomposition and the broadband power change across the high frequency range for each stimulus location, we obtain two time-courses per electrode, one for the alpha suppression (Equations 1,2) and one for the broadband elevation (Equation 3) (**Figure 3**). Each point in these time courses is a summary measure of a response component for a 500 ms stimulus presentation. Hence the time series are at very different scales from the ms voltage time series used to derive the summary measures.

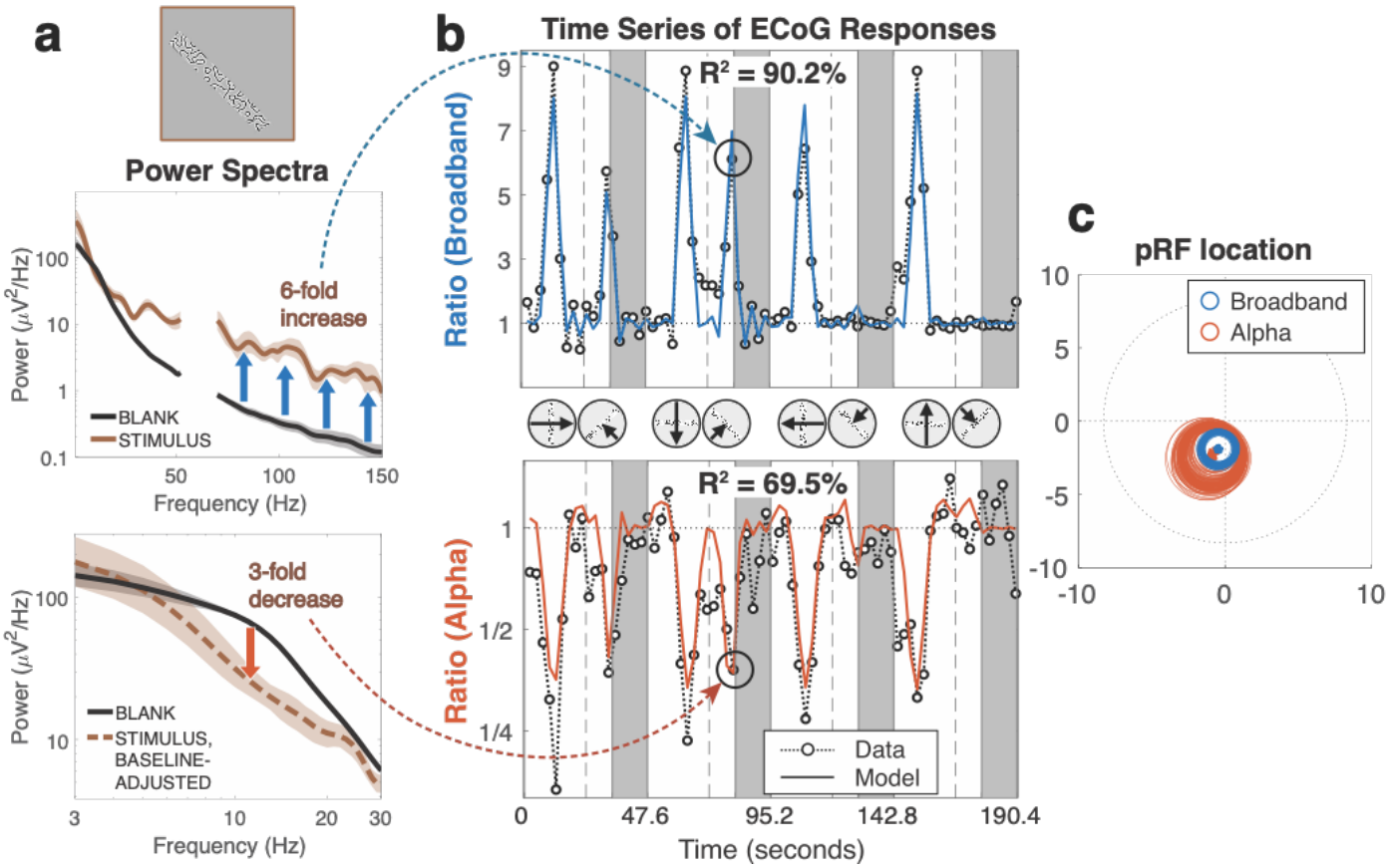

Figure 3. Example time series and pRF fits. Representative data from a V3 electrode ('GB103') from Patient 8. (**a**) The computation of broadband and alpha summary metrics for an example stimulus location. The power spectra were computed over 500 ms of stimulus presentations or blanks. The dashed brown line in the lower panel indicates spectral power for the stimulus after correcting for broadband shift. Shading represents the 68% bootstrapped confidence intervals across the 6 runs for STIMULUS and across 384 trials for BLANK, each with 1,000 resamples. (**b**) The time series of the broadband and alpha summary metrics averaged across six 190-s mapping runs, during which bar stimuli swept the visual field 8 times (with 4 blank periods indicated by the gray bars). Each data point (black circle) is a summary value –either broadband or alpha— for one stimulus position (Equations 1–3). Predicted responses from a pRF model are shown as solid lines. Model predictions below baseline in broadband and above baseline in alpha were possible because of the Difference of Gaussians (DoG) pRF model (see **Supplementary Figure 3-1**). (**c**) The location of the pRFs fitted to the broadband and alpha times series. The circles show the 1-sigma pRF bootstrapped 100 times across the 6 repeated runs. See *makeFigure3.m*.

After a small amount of pre-processing (averaging across repeated runs, temporal decimation, dividing out the mean response during the blanks), we separately fit pRF models to the broadband and the alpha time series (**Figure 3**). The pRF model we fit assumes linear spatial summation, with a circularly symmetric Difference of Gaussians (but constrained so that the surrounding Gaussian is large compared to the field of view of the experiment). Similar results were obtained using a model with compressive spatial summation or a model in which the surround size was allowed to vary.

In the example time series, it is evident that both components of the response vary with the stimulus position: for certain stimulus locations, the broadband response increased about 5- to 10-fold over baseline and the alpha response decreased about 3- to 5-fold. The pRF models accurately predicted these time series, with two-fold cross-validated variance explained of 90.2% for broadband and 69.5% for alpha. For both types of pRF, the center locations are in the parafovea in the left lower visual field, but the alpha pRF is about twice the size of the broadband pRF (**Figure 3**, right panel).

Next, we quantified the prediction accuracy of the pRF model fit across many electrodes, participants, and visual field maps. We first selected a large set of electrodes based only on location (see *Electrode Localization* in Methods 4.6). Electrodes were assigned to visual areas probabilistically. This implies that some electrodes were assigned to multiple visual areas, consistent with our uncertainty about localization. Probabilistic assignment results in high probability assignments getting more weight. We then grouped the electrodes based on whether or not we expected them to be visually responsive. Some of these electrodes are not expected to be visually responsive, for example, if their receptive field is beyond the stimulus extent. We identified visually responsive electrodes as those whose broadband pRF model accurately predicted the broadband time course (**Supplementary Figure 4-1**, left). Because the broadband quantification is limited to high frequencies (70–180 Hz), this criterion provides an independent means to separate the electrodes into groups to assess the alpha pRF model accuracy, which only depends on signals below 30 Hz.

We find that for visually selective electrodes in V1 to V3, the alpha pRF model explains 37% of the cross-validated variance in the alpha time series (**Figure 4**, "All Patients"). The non-visually selective electrodes provide a null distribution for comparison, and for these electrodes, the pRF model explains close to 0% of the variance. This pattern holds for individual patients with electrodes in V1–V3 (**Figure 4**, "Individual Patients"). In dorsolateral maps beyond V1–V3, the alpha pRF model explained about 24% of the variance in visually responsive electrodes, and no variance in the non-responsive group (**Supplementary Figure 4-2**).

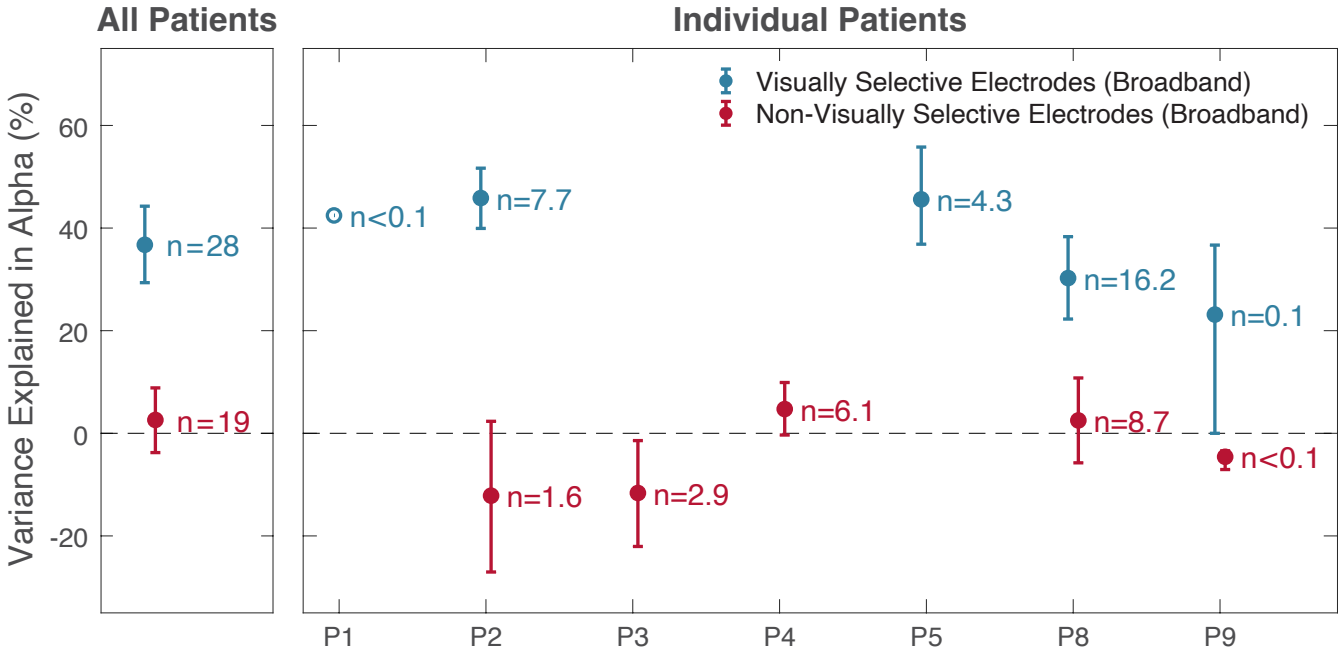

Figure 4. Prediction accuracy of alpha pRF models in V1–V3. The variance explained by alpha pRF models was higher in visually selective than non-visually selective electrodes. The left panel shows the results pooled across patients. The right side shows results from each patient separately. Two patients who didn't have electrodes in V1–V3 are not displayed. Visually selective electrodes were defined as those whose broadband pRF model accurately predicted the broadband time course (see **Supplementary Figure 4-1**). A similar pattern was observed for Dorsolateral maps beyond V1–V3 (**Supplementary Figure 4-2**). Electrodes were assigned to visual field maps probabilistically across 5,000 samples. Data points and error bars represent means ±1 standard deviation of the mean across the 5000 samples. An open dot includes only one electrode. See *makeFigure4_4S1_4S2.m*.

Overall, the difference in variance explained for the visually responsive vs non-visually response electrodes is many times larger than the variability across electrodes. These results show that across visual cortex, the pRF models explain a substantial part of the variance in the alpha time series.

2.4 The alpha pRFs are larger than broadband pRFs, but have similar locations

We next compared the alpha and broadband pRF parameters. We limited these comparisons to electrodes for which both signal types were well fit by pRF models (**Supplementary Figure 4-1**) and whose pRF centers were within the maximal stimulus extent (8.3°) for both broadband and alpha. Fifty-three electrodes met these criteria, of which 35 are assigned to V1–V3 and 45 to dorsolateral maps. (Because the assignments are probabilistic, 27 electrodes are assigned to both visual areas.)

As with the sample electrode (**Figure 3**), the center locations of the two pRF types tend to be close (**Figure 5a**). However, the alpha pRFs tend to be much larger and slightly more peripheral. The larger size of alpha pRFs is found in each patient and in nearly every electrode (15 of 17 for V1–V3, 34 of 36 for dorsolateral electrodes, associated with maximum probability; **Figure 5a, Supplementary Figure 5-1a**). Because the alpha pRFs are larger and the center locations are similar, the broadband pRFs are almost always contained within the alpha pRFs. Truncating the pRF sizes at 1 standard deviation, the percentage of the broadband pRF inside the alpha pRF was 92.3% (V1–V3) and 98.0% (dorsolateral) pRFs. This overlap is not a trivial consequence of the alpha pRFs simply being large. If we shuffle the relationship between alpha and broadband pRFs across electrodes, the overlap decreases sharply, to 30.0% (V1–V3) and 25.7% (dorsolateral). We summarized the relationship between the broadband and alpha pRFs by normalizing the parameters into a common space (**Figure 5b, Supplementary Figure 5-1b**) and then averaging pRFs across electrodes for both alpha and broadband. This analysis again confirms that the broadband pRF is, on average, smaller and less peripheral than the alpha pRF, and is mostly inside the alpha pRF.

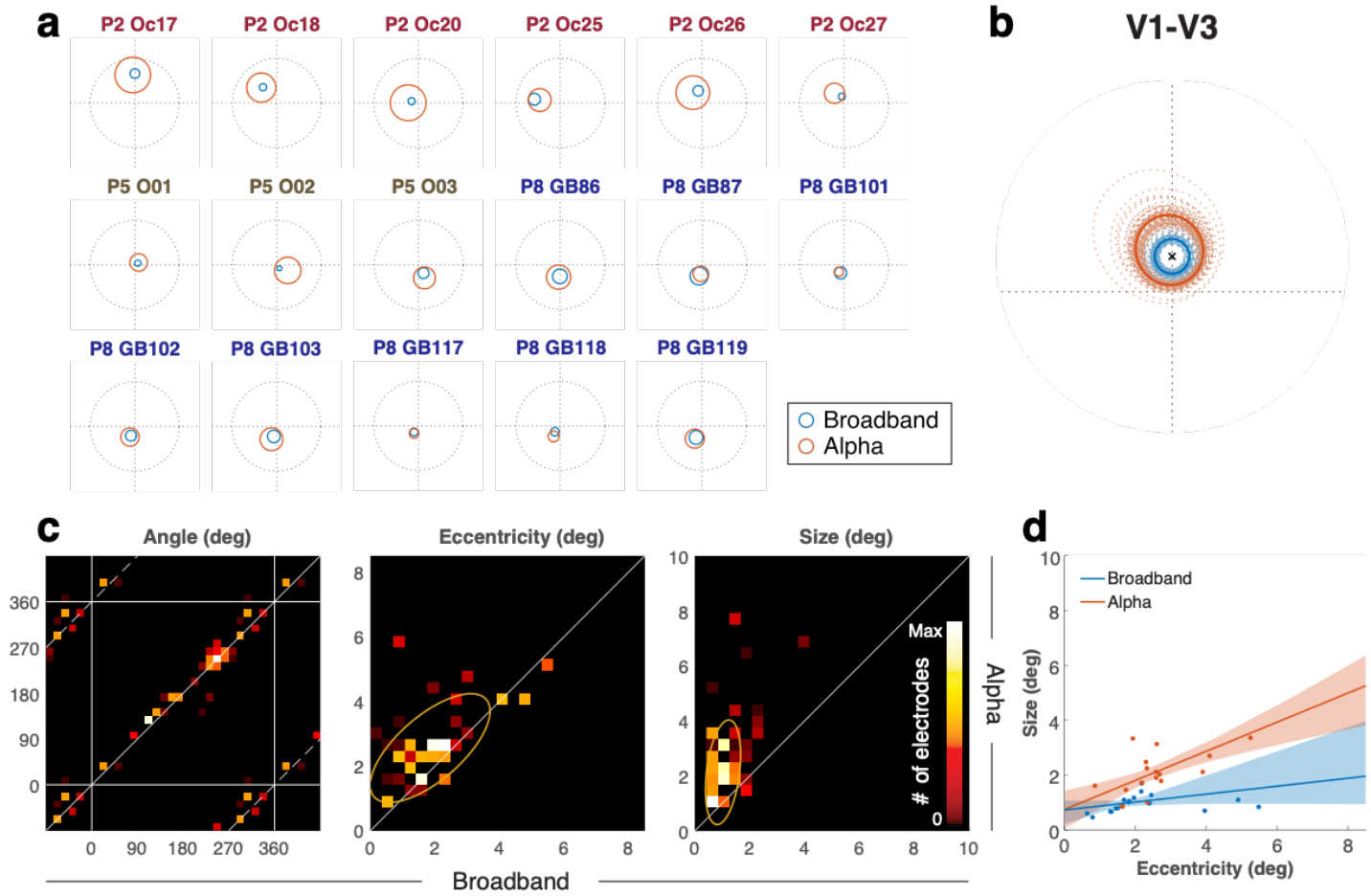

Figure 5. Relationship between alpha and broadband pRFs in V1–V3. (**a**) pRF locations in V1–V3 displayed for each electrode, as in **Figure 3**. For visualization purposes, only electrodes that are more likely to be assigned to V1–V3 than any other map are plotted, even though the probabilistic assignment (e.g. for panel c) included additional electrodes. (**b**) pRFs were normalized by rotation (subtracting the broadband pRF polar angle from both the broadband and alpha pRF) and then scaling (dividing the eccentricity and size of both pRFs by the broadband pRF eccentricity). This puts the broadband pRF center at (0,1) for all electrodes, indicated by an 'x'. Within this normalized space, the average pRF across electrodes was computed 5,000 times (bootstrapping across electrodes). 100 of these averages are indicated as dotted lines, and the average across all 5,000 bootstraps is indicated as a solid line. (**c**) Each panel shows the relation between broadband and alpha pRF parameters in 2-D histograms. 53 electrodes were randomly sampled with replacement 5,000 times (bootstrapping), and each time they were selected they were probabilistically assigned to a visual area. The colormap indicates the frequency of pRFs in that bin (see *Comparison of alpha and broadband pRFs* in Methods 4.7). Note that the phases in the horizontal and vertical axes are wrapped to show their circular relations. The middle and right panels show the relation of eccentricity and pRF sizes, respectively. Yellow ellipses indicate the 1-sd covariance ellipses. (**d**) The plot shows pRF size vs eccentricity, both for broadband (blue) and alpha (red). As in panel **c**, the 53 electrodes were bootstrapped 5,000 times. The regression lines are the average across bootstraps, and the shaded regions are the 16th to 84th percentile evaluated at each eccentricity. Electrodes that are more likely to be assigned to V1–V3 than any other maps are plotted as dots. (see **Supplementary Figure 5-1** for electrodes in dorsolateral maps). See *makeFigure5_5S1.m*.

In addition, a direct comparison of the alpha and broadband pRFs for each separate pRF model parameter (polar angle, eccentricity, size) reveals several patterns (**Figure 5c, Supplementary Figure 5-1c**). First, the polar angles are highly similar between broadband and alpha both in V1–V3 (r=0.98) and dorsolateral visual areas (r=0.95). Second, the eccentricities are correlated but not equal (r=0.68, 0.09): the alpha pRFs tend to have larger eccentricities than the broadband pRFs, especially in dorsolateral visual areas. Third, the sizes of alpha pRFs also correlate with those of broadband pRFs (r=0.33, 0.24), but are about 2–4 times

larger. These results suggest that the same retinotopic maps underlie both the alpha suppression and the broadband elevation, but that the alpha suppression pools over a larger extent of visual space. In the Discussion, we speculate about why the eccentricity of the alpha pRF might be systematically larger than the broadband eccentricity, even if the two signals originate from the same retinotopic map.

Our results also indicate that pRF size is much larger for alpha than for broadband. Because the comparison between alpha and broadband pRF size has such a steep slope (**Figure 5c**, right panel), one might wonder whether the size of the alpha pRFs vary in any meaningful way. Contrary to this possibility, we find that for both broadband pRFs and alpha pRFs, the pRF size systematically increases with eccentricity (**Figure 5d, Supplementary Figure 5-1d**), consistent with known properties of visual neurons (Newsome, Maunsell, & Van Essen, 1986) and with fMRI data (Dumoulin & Wandell, 2008; Kay, Winawer, Mezer, & Wandell, 2013). The slopes of the size vs. eccentricity functions are about 3 times larger for alpha than for broadband (slopes: 0.53 vs 0.15 in V1–V3; 1.17 vs 0.40 in dorsolateral, for alpha vs broadband).

2.5 The difference in pRF size is not due to a difference in temporal frequency

The larger pRF size for the alpha oscillation is not explained by the fact that the alpha band (8–13 Hz) is lower frequency than the band used to estimate the broadband signal (70–180 Hz). For V1 to V3, broadband power extended into low frequencies (**Supplementary Figure 6-1**), enabling us to quantify the spatial tuning of the low-frequency portion of the broadband response (3–26 Hz). Unlike the alpha pRFs, which had negative gain and a large size, the pRFs for the low frequency broadband response had a positive gain and a small size, similar to the high-frequency broadband response (sizes: 1.0 vs 1.1 vs 2.3 deg, for high-frequency broadband vs low-frequency broadband vs alpha; **Figure 6, Supplementary Figure 6-2**). The difference in size between low-frequency broadband and alpha pRFs suggest that the negative alpha modulations are not artifacts resulting from the baseline correction applied in our model-based approach.

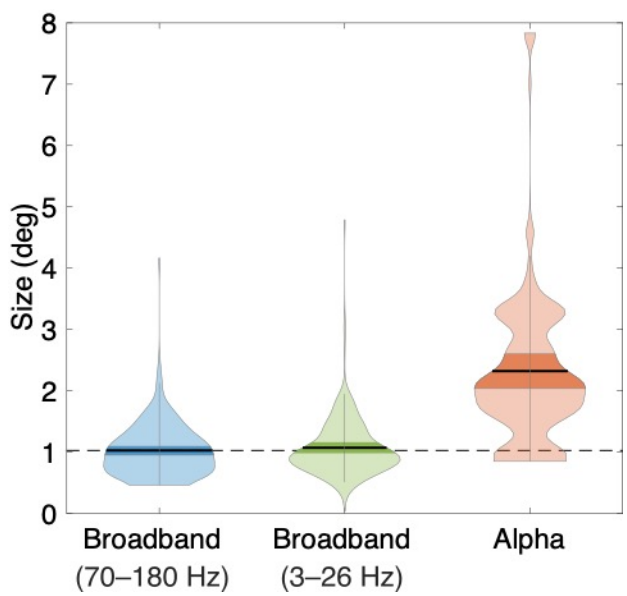

Figure 6. PRF sizes in broadband and alpha. Violin plots of pRF sizes with 5,000 bootstraps, estimated from high-frequency broadband, low-frequency broadband, and alpha. Black horizontal lines and dark color regions within violins indicate means ±1 standard deviation of the mean across the 5000 samples. A dotted horizontal line indicates the mean of high-frequency broadband pRF sizes. For the full power spectra showing the broadband and alpha responses, see **Supplementary Figure 6-1**. See *makeFigure6_6S2.m*.

2.6 The accuracy of the alpha pRFs depends on the baseline correction

We used a model-based approach to separate the alpha oscillatory power from the broadband response because the two responses overlap in temporal frequency. This model adjusts the baseline for computing alpha oscillatory power. Had we not used this approach, and instead used a more traditional method of computing band-limited power without a baseline correction, we would have obtained different values for the alpha responses and inaccurate pRF fits. The difference between the two methods is especially clear in V1–V3, where the broadband response extends into the low frequencies (**Supplementary Figure 6-1**). To clarify the advantage of the model-based approach, we compared the two types of pRF fits for all visually responsive electrodes in V1–V3 (based on maximum probability of map assignment: **Figure 7**). For these comparisons, we allowed the gain to be positive or negative. First, the cross-validated variance explained was about 4 times higher when correcting for the baseline (43% vs 10%, median). Second, as expected, the baseline-corrected approach consistently results in negative gain (29 out of 31 electrodes), meaning that alpha oscillations are suppressed by stimuli in the receptive field. In contrast, with no baseline correction, there is a mixture of positive and negative gain (14 negative, 17 positive), complicating the interpretation. Third, with baseline correction, pRF size increases with eccentricity, but without baseline correction it does not. These analyses confirm the importance of disentangling the alpha oscillation from the broadband response.

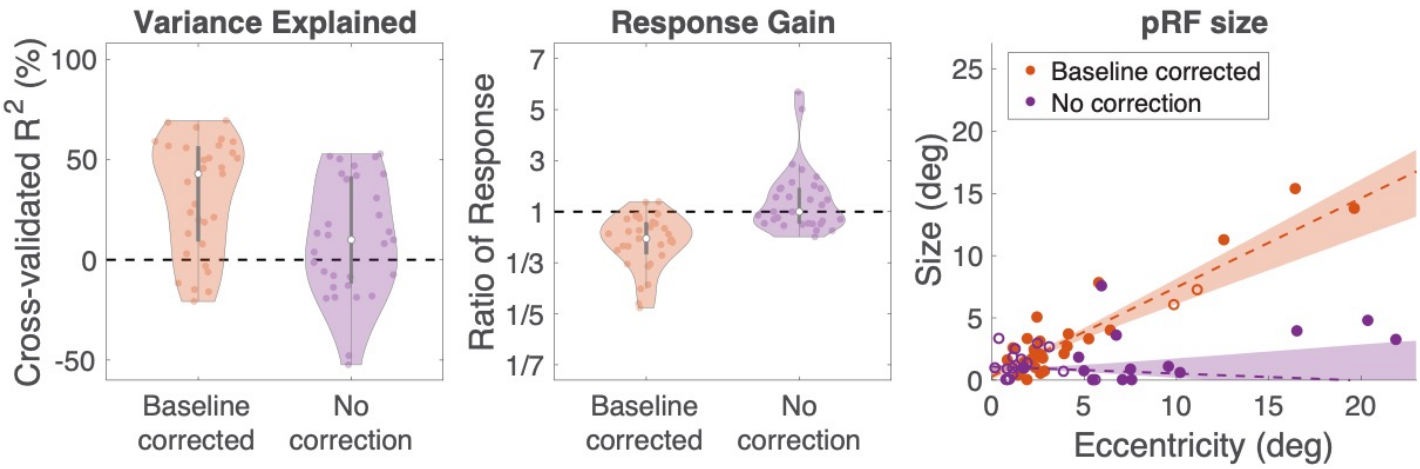

Figure 7. The advantage of baseline correction on alpha pRFs. We compared pRF solutions for alpha using our spectral model ("baseline corrected") vs by computing power within the alpha band ('no correction"). **Left**: Variance explained. The white dots are the median and the gray bars are the interquartile range. Each colored dot is one electrode and the shaded regions are smoothed histograms. **Middle**: Response gain, plotted in the same manner as variance explained. Gain is quantified as the maximum or minimum value in the pRF fitted time series (maximal for electrodes with positive gain, minimal for electrodes with negative gain). A value above 1 means that the response increased relative to baseline (positive gain). A value below 1 means the response decreased (negative gain). **Right**: pRF size vs eccentricity. Electrodes are colored by the sign of the gain (filled for negative, open for positive). These tendencies are consistent across individual patients (**Supplementary Figure 7-1**). The shadings represent 68% bootstrapped confidence intervals with 1,000 resamples. See *makeFigure7_7S1.m*.

2.7 Alpha oscillations are coherent across a larger spatial extent than broadband signals

The large pRFs for alpha suppression might result from a limit to the spatial resolution at which alpha oscillations can be controlled. If, for example, alpha oscillations are up- or down-regulated with a point spread function of ~5 or 10 mm of cortex, then alpha pRFs would necessarily be large. We assessed the

spatial resolution of the alpha oscillation by measuring coherence of the signal across space. Specifically, we measured coherence at the alpha frequency for electrode pairs in two high-density grids (Patients 8 and 9; See **Supplementary Figures 8-1 and 8-2** for pRF parameters on the two high-density grids). These grids have 3 mm spacing between electrodes, about 10 times the density of standard grids (1 cm spacing). For comparison, we also measured the coherence between the same electrode pairs averaged across the frequencies we used for calculating broadband responses (70 Hz to 180 Hz).

We find two clear patterns as shown in **Figure 8**. First, as expected, coherence declines with distance. The alpha coherence is about 0.6 between neighboring electrodes, declining to a baseline level of about 0.35 by about 1 cm. Second, the coherence was higher at the alpha frequency than in the broadband frequencies, especially between neighboring electrodes. The pattern is the same whether the coherence is computed only from trials in which the bar position overlapped pRF, or only from trials in which it did not overlap the pRF, or both (data not shown.) Overall, the larger coherence at the alpha frequency is consistent with coarser spatial control of this signal (in mm of cortex), and larger pRFs (in deg of visual angle). The highest coherence is at the peak alpha frequency (**Supplementary Figure 8-3**). This suggests that the elevated coherence is not simply an artifact of greater volume conduction at low frequencies.

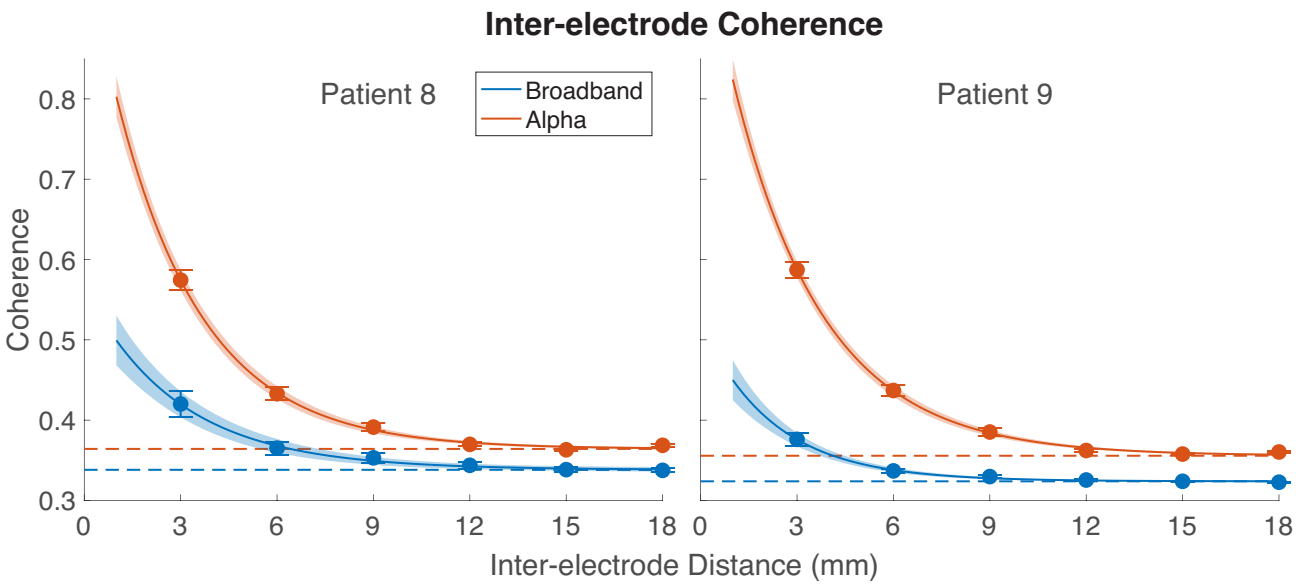

Figure 8. Inter-electrode coherence across distances in high-density grids. Coherence between electrode pairs was computed within each 1-s epoch and then averaged epochs. Seed electrodes were those which had a reliable pRF fit, and these seed electrodes were compared to all other electrodes on the grid. The curved lines indicate the average fit of an exponential decay function across 5,000 bootstraps; shading indicates ±1 standard deviation of bootstraps; dashed lines indicate the baselines the coherence converges to. See **Supplementary Figure 8-3** for coherence as a function of frequency. See *makeFigure8.m*.

3. Discussion

Our main two findings are that visual cortex alpha suppression is specific to stimulus location, as measured by its pRF, and that alpha pRFs are more than twice the size of broadband pRFs. This supports that alpha suppression in and near the locations of the driven response increases cortical excitability. This has implications for visual encoding in cortex, perception, and attention, with several close parallels between the alpha pRF and exogenous (stimulus-driven) attention.

3.1 What is the function of the large alpha pRFs?

The alpha oscillation was originally characterized as an "idling" or default cortical state, reflecting the absence of sensory input or task demand (Adrian & Matthews, 1934; Barry et al., 2007; Berger, 1929; Klimesch, Doppelmayr, Russegger, Pachinger, & Schwaiger, 1998; Matousek & Petersen, 1983). However, more recent work supports the idea that alpha oscillations act as a gate, actively suppressing neural signals by reducing cortical excitability (Bastos, Lundqvist, Waite, Kopell, & Miller, 2020; Jensen & Mazaheri, 2010; Klimesch, Sauseng, & Hanslmayr, 2007; Mazaheri & Jensen, 2010; Van Diepen, Foxe, & Mazaheri, 2019) via "pulsed inhibition" (hyperpolarization followed by rebound). This pulsed inhibition explains why cortical excitability depends on both alpha oscillation *magnitude* (Kelly et al., 2006; Rihs et al., 2007; Worden et al., 2000) and *phase* (Osipova, Hermes, & Jensen, 2008; Spaak, de Lange, & Jensen, 2014): when the oscillations are large, there is one phase when cortex is most excitable and one phase when it is least excitable (phase dependence), and when the oscillations are small, cortex is on average more excitable (magnitude dependence). When coupled to the large pRFs, this predicts that the onset of a focal visual stimulus will cause an increase in cortical excitability, spreading beyond the region that responds directly, i.e., with broadband field potentials and spiking (Error! Reference source not found.). A transient increase in excitability spreading beyond the stimulus is conceptually similar to stimulus-driven ("exogenous") spatial attention, in which a visual cue leads to faster response times, increased discriminability, higher perceived contrast (Carrasco, 2011; Downing & Pinker, 1985; Shulman, Sheehy, & Wilson, 1986), and increased neural response, as measured by single unit spike rates (F. Wang, Chen, Yan, Zhaoping, & Li, 2015) and BOLD fMRI (Dugue, Merriam, Heeger, & Carrasco, 2020).

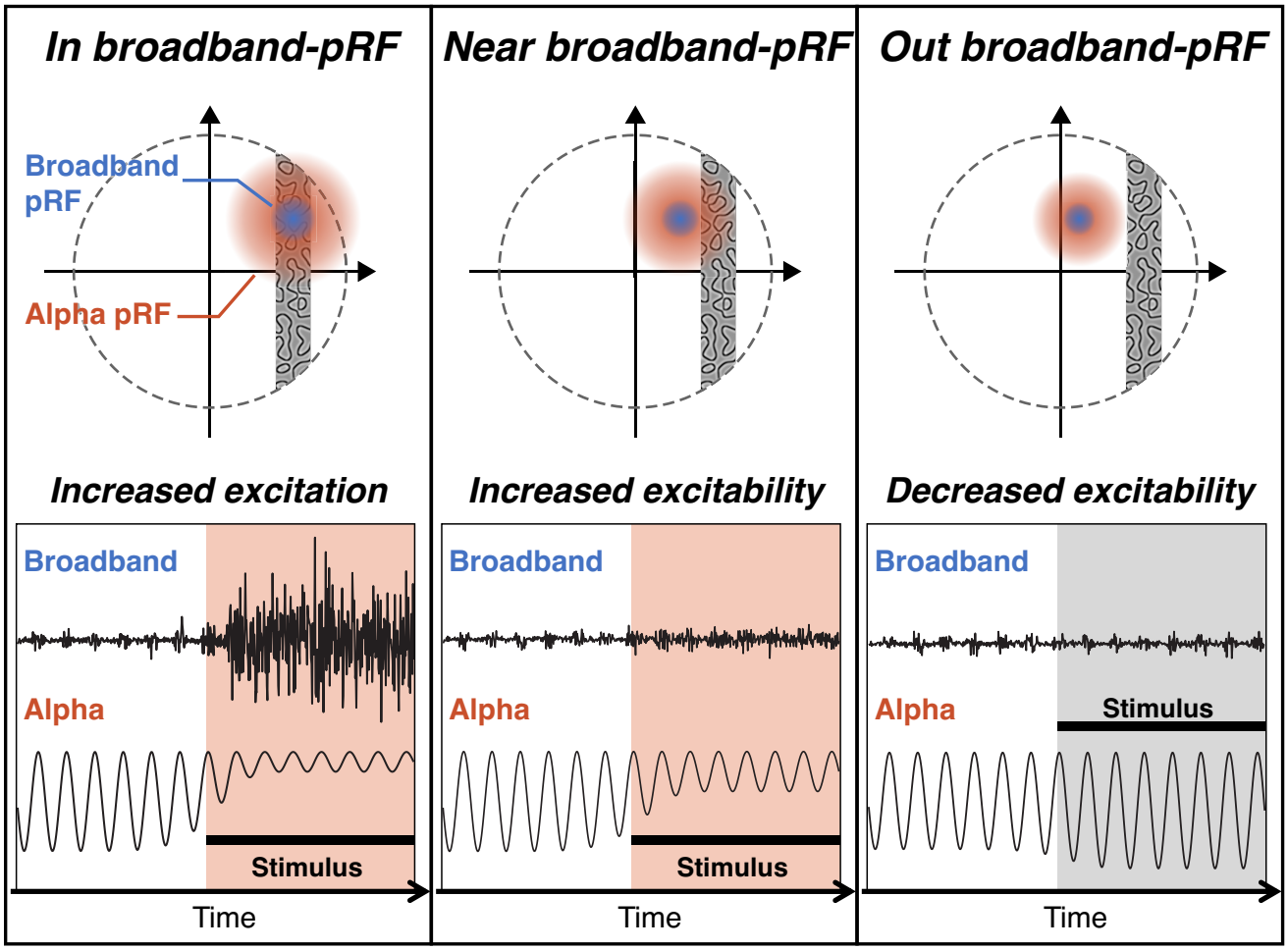

Figure 9. Schematics of neural excitation and excitability changes induced by visual stimulation. The upper panels show stimulus position relative to the broadband and alpha pRFs for a given electrode. The lower panel shows predicted alpha and broadband responses from that electrode, with stimulus onset indicated by the black horizontal bar. In the left and middle panels, the stimulus causes the alpha oscillations to be suppressed and cortex to become more excitable (red shading). In the right panel, the alpha oscillation increases slightly and cortex becomes less excitable (gray shading).

The relationship may be more than conceptual, however, as we find that the spatial profiles of attention, measured behaviorally (Downing & Pinker, 1985; Shulman et al., 1986), and of the alpha pRF are quite similar (**Figure 10**), with three close parallels. For both measures, the spatial spread (1) increases with eccentricity, (2) is asymmetric, spreading further into the periphery than toward the fovea, and (3) shows center/surround organization, with the attentional effect changing from a benefit to a cost and the alpha response changing from suppression to enhancement. The timing also matches, since exogenous attention has a maximal effect at about 100 ms (Nakayama & Mackeben, 1989; F. Wang et al., 2015), the duration of an alpha cycle.

While many studies have proposed that attention, whether stimulus driven (exogenous) or internal (endogenous), influences the alpha oscillation (Foster et al., 2017; Kelly et al., 2006; Popov et al., 2019; Rihs et al., 2007; Samaha et al., 2016; Sauseng et al., 2005; Worden et al., 2000), our proposal flips the causality. We propose that the stimulus causes a change in the alpha oscillation and this in turn causes increased neural responsivity and behavioral sensitivity, the hallmarks of covert spatial attention. The spatial spread of the alpha oscillation can be traced in part to the neural mechanisms generate it in the thalamus (see section *3.2*). Top-down attention may capitalize on some of the same mechanisms, as feedback to the LGN can modulate

the alpha-initiating neural populations, then resulting in the same effects of cortical excitability in visual cortex that occur from bottom-up spatial processing. This is consistent with findings that endogenous attention is accompanied by local reductions in alpha oscillations (Popov et al., 2019; Sauseng et al., 2005; Worden et al., 2000).

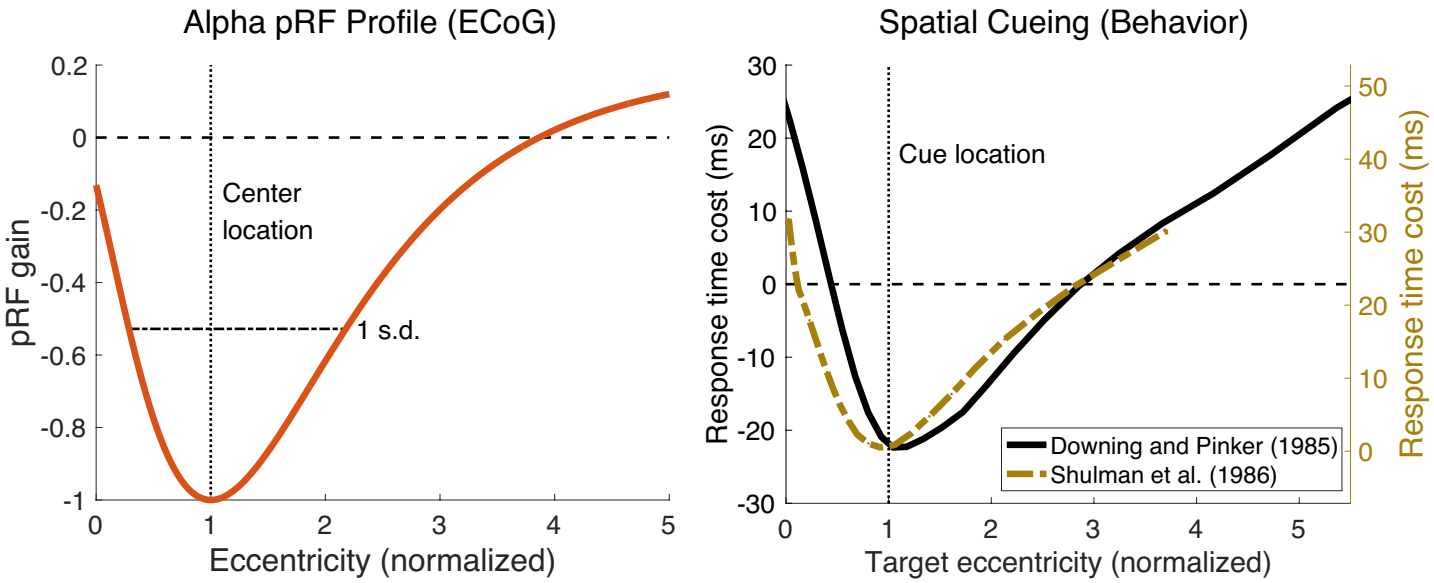

Figure 10. Asymmetric profile of alpha pRF and asymmetric effect of spatial attention. The left panel shows an asymmetric profile of alpha pRF across normalized eccentricity in V1–V3. The right panel shows asymmetric effects of attention on normalized cue–target locations. Black line represents response time changes induced by endogenous attention from Downing and Pinker [30], relative to the response time without any attentional cue. The gold line represents response time changes induced by exogenous attention from Shulman et al. [29], relative to the response time when targets appeared at the attended locations. Results from the Shulman et al. paper with foveal cue locations at 0.5 degree eccentricity were excluded from the plot because after normalizing, the data from this condition has no overlap with the other conditions perhaps because at such a small eccentricity, a minor error in attended location makes a large difference on a normalized scale. The experimental results for each cue location are shown in **Supplementary Figure 10-1**. See *makeFigure10.m*.

This link to attention contrasts with the proposal that the alpha oscillation in visual cortex reflects surround suppression (Harvey et al., 2013). We think the alpha oscillation is not tightly linked to surround suppression. First, the alpha pRF is negative, and alpha tends to be inhibitory (Bastos et al., 2020; Jensen & Mazaheri, 2010; Klimesch et al., 2007; Mazaheri & Jensen, 2010; Van Diepen et al., 2019), meaning that visual stimuli within the alpha pRF disinhibit cortex, the opposite of surround suppression. An excitatory surround (alpha suppression) and a suppressive surround can coexist if they differ in timing and feature tuning. Surround suppression is relatively fast, disappearing 60 ms after surround stimulus offset (Bair, Cavanaugh, & Movshon, 2003) whereas the ~10 Hz alpha oscillation is likely to be modulated at a slower time scale. Furthermore, surround suppression is feature-specific (Bair et al., 2003), whereas the alpha oscillation, being coherent over several mm of cortex, is unlikely to be limited only to cells whose tuning match the stimulus. Nonetheless surround suppression may be linked to neural oscillations, albeit at a higher frequency range (Hermes, Petridou, Kay, & Winawer, 2019; Ray, Ni, & Maunsell, 2013).

Other studies have proposed that retinotopically specific alpha oscillations are related to oculomotor behavior (Popov, Langer, Gips, Weisz, & Jensen, 2021; Popov, Miller, Rockstroh, Jensen, & Langer, 2021). Supporting evidence includes the observations that oscillations decrease with saccade initiation (Popov, Miller, et al., 2021) and that saccades can be phase-locked to the alpha rhythm (Drewes & VanRullen, 2011; Staudigl, Hartl, Noachtar, Doeller, & Jensen, 2017). In our study, participants maintained fixation at the

center of the screen during receptive field mapping, dissociating modulations in the alpha oscillation from large eye movements. Nonetheless, there are many parallels, and likely shared circuitry, between spatial attention and eye movements (Moore & Fallah, 2001; Shepherd, Findlay, & Hockey, 1986).

An alternative interpretation of our results is that the larger alpha pRFs are an artifact of lower signal-to-noise ratio. We think this is unlikely for three reasons. First, simulations of pRFs in which the ground truth is known show no systematic increase in pRF size with more noise (Lerma-Usabiaga, Benson, Winawer, & Wandell, 2020, their figure 8). Second, adding substantial noise to real fMRI data had little to no effect on pRF size (Le, Witthoft, Ben-Shachar, & Wandell, 2017, their figure 6). Third, the larger size of the alpha pRFs is preserved when regressing size vs variance explained (

Supplementary Figure 5-2).

We focused on the spatial specificity of alpha oscillations on the cortical surface. A separate line of research has also examined the specificity of alpha oscillations in terms of cortical depth and inter-areal communication. One claim is that oscillations in the alpha and beta range play a role in feedback between visual areas, with evidence from nonhuman primates for specificity of alpha and beta oscillations in cortical depth (Bastos et al., 2020; Bollimunta, Mo, Schroeder, & Ding, 2011). To our knowledge, no one has examined the spatial specificity of the alpha oscillation across the cortical surface and across cortical depth in the same study, and it remains an open question as to whether the same neural circuits are involved in both types of effects.

3.2 The importance of separating oscillatory and non-oscillatory signals

Separating the alpha power into oscillatory and broadband components was motivated by the different biological origins of the two signals. Recent work has identified a population of high threshold thalamocortical neurons that generates bursts in the alpha or theta frequency range (depending on membrane potential) (Hughes & Crunelli, 2007; Hughes et al., 2011; Lorincz, Kekesi, Juhasz, Crunelli, & Hughes, 2009). These bursts are synchronized by gap junctions. These neurons themselves appear to be the pacemakers, generating the alpha rhythm in the LGN and transmitting it to V1. This explains the rhythmic nature of the signal (bursting), the coherence across space (synchrony by gap junctions), and the occipital locus of alpha (thalamocortical generators). The fact that this cell population is located in the LGN does not imply that the alpha oscillation is only based on feedforward signals. Feedback signals from V1 to LGN via corticothalamic cells can modulate the frequency and amplitude of the alpha generating thalamocortical cells (Hughes & Crunelli, 2007). There may also be intracortical circuits that modulate the alpha oscillation (Bollimunta et al., 2011; Clayton, Yeung, & Cohen Kadosh, 2018).

The broadband response differs in several ways. First and most obvious, the signal is not limited to a narrow frequency range (Hermes, Miller, Wandell, & Winawer, 2015; Hermes et al., 2017; Hermes et al., 2019; Miller, Sorensen, et al., 2009; Winawer et al., 2013), and hence is not generally considered an oscillation (Miller et al., 2014). Therefore, functions which are hypothesized to depend specifically on oscillations should likely not be imputed to this signal, such as a behavioral bias during certain phases of the oscillation (Busch, Dubois, & VanRullen, 2009; Mathewson, Gratton, Fabiani, Beck, & Ro, 2009; Spaak et al., 2014) or long range synchronization of signals (Palva & Palva, 2011, 2012). Second, broadband signal are found throughout the brain (Kupers et al., 2018; Manning et al., 2009; Miller et al., 2014), likely arising from non-oscillatory neural generators (Bedard, Kroger, & Destexhe, 2006; Miller, Sorensen, et al., 2009), whereas the alpha rhythm is largest in the occipital lobe. Finally, the broadband signal measured at the electrode has lower amplitude because the generators are not synchronized across space.

The motivation to separate the signals was confirmed by the results. Compared to the frequency band method (no decomposition), the decomposition method resulted in higher variance explained, more consistent direction (negative pRFs rather than a mixture of positive and negative), and a tighter relationship between pRF eccentricity and size. The frequency band method has poorer results because it conflates two signals with different properties.

The difference between the methods likely explains some discrepancies across studies. Klink et al. (2021) fit pRF models to electrode data from macaque primary visual cortex in many frequency bands, including alpha, without removing the broadband signal. They found no systematic relationship between pRF size and eccentricity and found that the gain was positive for some electrodes and negative for others. The interpretation was that some locations in the visual field show suppression and others excitation. Our results suggest that it is more likely that most or all locations show both responses, alpha suppression and broadband increase, with either of the two signals sometimes being larger. Second, Takaura et al. (2016) estimated receptive fields in macaque in several frequency bands, including alpha. They found that alpha power tended to increase by visual stimulation, in contrast to our results. We speculate that visual stimuli decreased alpha oscillations, but that this decrease was masked by a larger broadband power increase. Finally, Harvey et al. (2013) examined spatial selectivity of human ECoG responses in the alpha band. They fit pRF models to the broadband response and then measured alpha power for stimulus positions relative to the broadband pRFs. They reported that alpha power increased in V1 electrodes when stimuli were outside the pRF, and that there was no change in alpha power when the stimulus overlapped the broadband pRF. The combination of these two results led to an interpretation that the alpha response is specifically related to surround suppression. Our results confirm their first observation that alpha power increases when the stimulus is outside the pRF (as reflected in our Difference of Gaussians model); however, in contrast to their report, we find strong alpha suppression when the stimulus is in the pRF center. The discrepancy is reconciled by the approach. We, too, find that total alpha power is approximately unchanged by the stimulus in the pRF center, but the model-based approach shows that this is due to cancellation from an increased broadband response and a reduced alpha oscillation, rather than to the alpha oscillation not changing.

A similar decomposition approach was used in prior ECoG studies to separate broadband power from steady state visual evoked potentials (Winawer et al., 2013) and from narrowband gamma oscillations (Hermes et al., 2015; Hermes et al., 2017; Hermes et al., 2019). A generalization of this approach has also been implemented in a toolbox for separating broadband and narrowband signals (Donoghue et al., 2020). These approaches are premised on the idea that different signals arise from different neurobiological causes and may be modulated independently by stimulus or task. This contrasts with the tradition of separating the field potential into frequency bands, where band-limited power is often computed without identifying a spectral peak and without removing non-oscillatory contributions.

One potential concern about our approach might be circularity: is it possible that we found the alpha and broadband signals to have opposite signs and similar pRF locations because there is in fact only one independent neural response, which we projected onto two measures? We think this is not the case. First, the broadband and the alpha power changes fitted by the pRF model were computed in different frequency ranges so that they were mathematically independent: the broadband was computed in high frequency range (70–180 Hz) and the alpha was decomposed from the low-frequency broadband response in 3–26 Hz (or 3–32 Hz). Second, if the two responses arose from one independent signal, then both the center locations and the sizes of alpha and broadband pRFs would be the same, but the alpha pRFs were much larger than the broadband pRFs.

The advantage of our approach is not limited to the visual system. Alpha suppression is observed in other cortical areas (https://onlinelibrary.wiley.com/doi/full/10.1111/ejn.13747), as are broadband responses (Miller 2014), and hence the need for spectral modeling is likely to be widespread.

3.3 How broad is broadband?

Since Crone et al.'s (1998) observations of task related power increases at high frequency (70–100 Hz, above the typical gamma band), there has been a great deal of interest in these high frequency signals. Unlike the lower frequency gamma oscillations studied previously (Eckhorn et al., 1988; Gray & Singer, 1989), the signals above 70 Hz had no clear peak. Crone et al. speculated that this was due to the ECoG signal pooling across multiple oscillatory circuits with different peak frequencies. Signal changes above 70 Hz have been referred as "high gamma" (Bartoli et al., 2019; Brovelli, Lachaux, Kahane, & Boussaoud, 2005; Canolty et al., 2006; Ray & Maunsell, 2011), implicitly conveying that the signals are similar to gamma oscillations, but just at a higher frequency.

In contrast, Miller et al. (2009) proposed that these signals, although appearing to be concentrated in high frequencies, do not in fact arise from neural oscillations at all. They interpreted these signals as reflecting broadband neural activity with no specific time scale, spanning the whole spectrum but obscured at lower frequencies by changes in narrowband phenomena (Miller, Zanos, Fetz, den Nijs, & Ojemann, 2009). Such task-related broadband power increases have been found in human intracranial electrodes over V1 to V3 (Winawer et al., 2013) and in human microelectrode recordings of local field potentials (Manning et al., 2009). Our results confirm their findings as the broadband increase is observed from as low as 3 Hz in V1–V3. The broadband responses in low-frequency (3–26 Hz) and high-frequency band (70–180 Hz) showed similar response patterns to the pRF stimuli, as reflected in similar pRF model parameters, suggesting they have a common cause.

There may, however, be variability across cortical locations (and across people) in the neural circuit properties that generate broadband responses. We find a difference in the pattern between V1–V3 and the dorsolateral maps. In V1–V3, the stimulus-related broadband elevation is clear all the way down to 3 Hz or lower, whereas in dorsolateral cortex it is clear only down to about 25 Hz. The difference could reflect fundamental differences in the type of field potentials that can be generated from the two regions, or could depend on how well matched the stimuli are to the tuning of the brain areas: the simple contrast patterns used for pRF mapping more effectively drive the early visual field maps than higher level areas (e.g., producing twice the percent signal change in high broadband signals). The human microelectrode recordings (Manning et al., 2009) indicate that broadband power extending as low as 2 Hz can be measured across many brain regions, including frontal, parietal, and occipital cortices as well as hippocampus and amygdala. A further consideration is that broadband power changes might entail changes in the exponent of the spectral power function in addition to a change in the scaling (Donoghue et al., 2020). In either case, however, it is likely that the power changes in high frequency regions reported here and elsewhere (e.g., Miller et al., 2014) reflect processes which are not oscillatory and hence not limited to a narrow range of frequencies. And because the model-based method of quantifying alpha oscillations shows a clear advantage for some regions (V1–V3) and no disadvantage for others, it is a more interpretable and general method than simply measuring the power at a particular frequency.

3.4 Conclusion

With high spatial precision measurements, we have demonstrated that there are two independent responses to visual stimulation in the alpha band: suppression of alpha oscillations and elevation of broadband power. Separating the two responses was essential for accurately fitting pRF models to the alpha oscillation. The large, negative alpha pRF indicates that visual stimulation suppresses alpha oscillations and likely increases cortical excitability over a large cortical extent (larger than the region with broadband and spiking increases). Together, these results predict many of the effects observed in spatial cueing experiments, thus providing further links between the alpha oscillation and spatial attention. More generally, alpha oscillation is likely to play a role in how cortex encodes sensory information.

4. METHODS

The dataset was collected as part of a larger project funded by the NIH (R01MH111417). The methods for collecting and preprocessing the visual ECoG data have been described recently (Groen et al., 2022). For convenience, data collection methods below duplicate some of the text from the methods section of Groen et al. (2022) with occasional modifications to reflect slight differences in participants, electrode selection, and pre-processing.

4.1 DATA AND CODE AVAILABILITY

All data and code are freely available. We list the main sources of data and code here for convenience: The data are shared in BIDS format via Open Neuro (https://openneuro.org/datasets/ds004194). The analysis depends on two repositories with MATLAB code: one for conversion to BIDS and pre-processing (ECoG_utils, https://github.com/WinawerLab/ECoG_utils), and one for analysis of the pre-processed data (ECoG_alphaPRF, https://github.com/KenYMB/ECoG_alphaPRF). The analysis also has several dependencies on existing public tools, including analyzePRF (Kay, Winawer, Mezer, et al., 2013) (https://github.com/cvnlab/analyzePRF), FieldTrip (Oostenveld, Fries, Maris, & Schoffelen, 2011) (https://github.com/fieldtrip/fieldtrip), and FreeSurfer (http://freesurfer.net). Within the main analysis toolbox for this paper (ECoG_alphaPRF), there is a MATLAB script to re-generate each of the main data figures in this paper, called '*makeFigure1.m*', '*makeFigure2.m*', etc. Sharing both the raw data and the full set of software tools for analysis and visualization facilitates computational reproducibility and enables inspection of computational methods to a level of detail that is not possible from a standard written Methods section alone.

All code used for generating the stimuli and for experimental stimulus presentation can be found at https://github.com/BAIRR01/BAIR_stimuli and https://github.com/BAIRR01/vistadisp.

4.2 PARTICIPANTS

ECoG data were recorded from 9 participants implanted with subdural electrodes for clinical purposes. Data from 7 patients were collected at New York University Grossman School of Medicine (NYU), and from 2 patients at the University Medical Center Utrecht (UMCU). The participants gave informed consent to participate, and the study was approved by the NYU Grossman School of Medicine Institutional Review Board and the ethical committee of the UMCU. Detailed information about each participant and their implantation is provided in **Table 1**. Two patients (p03 and p04) were not included because they did not participate in the pRF experiment which we analyzed for the purpose of the current study.

Patient	BIDS Code	Age	Sex	Site	PRF runs	Hemi	Implantation	Coverage	# of Visual	Matching areas with maximum probability
Patient 1	p01	30	F	UMCU	4	L	strip, depth	lat-occ, lat-par, vent-temp	8	PHC, V3AB, LO, TO
Patient 2	p02	18	F	UMCU	2	R	grid, strip	med-occ, lat-occ, lat-temp, vent-temp	20	V1, V2, V3, hV4, V3AB, TO, IPS
Patient 3	p05	31	F	NYU	4	R	2× grid, strip, depth	lat-occ, lat-par, frontal, ant-temp	21	V2, V3, hV4, LO, TO, IPS
Patient 4	p06	19	F	NYU	2	L	grid, strip, depth	med-occ, lat-occ, lat-par, ant-temp, frontal	28	V1, V2, V3, hV4, V3AB, LO, TO, IPS
Patient 5	p07	41	F	NYU	4	L	grid, strip, depth	lat-occ, lat-par, med-occ, ant-temp, frontal	20	V1, V2, V3, V3AB, TO, IPS
Patient 6	p08	47	F	NYU	2	R	grid, strip, depth	lat-par, ant-temp	6	LO, TO, IPS
Patient 7	p09	25	M	NYU	4	L,R	bilateral grid, strip, depth	lat-occ, lat-par	8	LO, TO, IPS
Patient 8	p10	23	M	NYU	6	R	grid, HD grid, strip, depth	lat-occ, lat-par, post-vent	130	V2, V3, V3AB, LO, TO, IPS, SPL
Patient 9	p11	19	F	NYU	6	L	grid, HD grid, strip, depth	lat-occ, lat-par, post-vent	93	hV4, VO, V3AB, LO, TO, IPS

Table 1. Overview of patient data included in this dataset. The patient number and subject code for BIDS do not always match because the 9 subjects with pRF data are a subset of 11 subjects from a larger BIDS dataset (https://openneuro.org/datasets/ds004194). Two of the 11 patients did not take part in pRF experiments.

4.3 ECoG RECORDINGS

NYU

Stimuli were shown on a 15 in. MacBook Pro laptop. The laptop was placed 50 cm from the participant's eyes at chest level. Screen resolution was 1280 × 800 pixels (33 × 21 cm). Prior to the start of the experiment, the screen luminance was linearized using a lookup table based on spectrophotometer measurements (Cambridge Research Systems). ECoG data were recorded using four kinds of electrodes: Standard size grids, linear strips, depth electrodes, and high-density grids, with the following details.

- Standard grids (8 × 8 arrays) and strips (4 to 12 contact linear strips) were implanted, consisting of subdural platinum-iridium electrodes embedded in flexible silicone sheets. The electrodes had 2.3-mm diameter exposed surface and 10-mm center-to-center spacing (Ad-Tech Medical Instrument, Racine, Wisconsin, USA).
- Penetrating depth electrodes (1 × 8 or 1 × 12 contacts) were implanted, consisting of 1.1-mm diameter electrodes, 5- to 10-mm center-to-center spacing (Ad-Tech Medical Instrument).
- In two patients (Patient 8 and 9), there were small, high-density grids (16 x 8 array) implanted over lateral posterior occipital cortex. These high-density grids were comprised of electrodes with 1-mm diameter exposed surface and 3-mm center-to-center spacing (PMT Corporation, Chanhassen, Minnesota, USA).

Recordings were made using one of two amplifier types: NicoletOne amplifier (Natus Neurologics, Middleton, WI), bandpass filtered from 0.16–250 Hz and digitized at 512 Hz, and Neuroworks Quantum Amplifier (Natus Biomedical, Appleton, WI) recorded at 2048 Hz, bandpass filtered at 0.01–682.67 Hz and then downsampled to 512 Hz. Stimulus onsets were recorded along with the ECoG data using an audio cable connecting the laptop and the ECoG amplifier. Behavioral responses were recorded using a Macintosh wired external numeric keypad that was placed in a comfortable position for the participant (usually their lap) and connected to the laptop through a USB port. Participants self-initiated the start of the next experiment by pushing a designated response button on the number pad.

UMCU

Stimuli were shown on an NEC MultiSync® E221N LCD monitor positioned 75 cm from the participant's eyes. Screen resolution was 1920 x 1080 pixels (48 x 27cm). Stimulus onsets were recorded along with the ECoG data using a serial port that connected the laptop to the ECoG amplifier. As no spectrophotometer was available at the UMCU, screen luminance was linearized using the built-in gamma table of the display device. Data were recorded using the same kinds of electrodes as NYU: Standard grids and strips, and depth electrodes, and using a MicroMed amplifier (MicroMed, Treviso, Italy) at 2048 Hz with a low-pass filter of 0.15Hz and a high-pass filter of 500Hz. Responses were recorded with a custom-made response pad.

4.4 pRF Stimulus

Visual stimuli were generated in MATLAB 2018b. Stimuli were shown at 8.3 degrees of visual angle (16.6 degrees stimulus diameter) using Psychtoolbox-3 (http://psychtoolbox.org/) and were presented at a frame rate of 60 Hz. Custom code was developed in order to equalize visual stimulation across the two recording sites as much as possible; for example, all stimuli were constructed at high resolution (2000 x 2000 pixels) and subsequently downsampled in a site-specific manner such that the stimulus was displayed at the same visual angle at both recording sites (see *stimMakePRFExperiment.m* and *bairExperimentSpecs.m* in BAIRR01/BAIR_stimuli). Stimuli consisted of grayscale bandpass noise patterns that were created following procedures outlined in Kay et al. (2013). Briefly, the pattern stimuli were created by low-pass filtering white noise, thresholding the result, performing edge detection, inverting the image polarity such that the edges are black, and applying a band-pass filter centered at 3 cycles per degree (see *createPatternStimulus.m*).

All stimuli were presented within bar apertures; the remainder of the display was filled with neutral gray. This stimulus has been shown to effectively elicit responses in most retinotopic areas (Kay, Winawer, Rokem, Mezer, & Wandell, 2013). The width of the bar aperture was 2 degrees of visual angle, which was 12.5% of the full stimulus extent. The bar aperture swept across the visual field in eight directions consisting of twenty-eight discrete steps per sweep, 850 ms step duration. During each step, the bar stimulus was displayed for 500 ms followed by a 350 ms blank period showing a gray mean luminance image. The eight sweeps included 2 horizontal (left to right or right to left), 2 vertical (up to down or down to up) and 4 diagonal sweeps (starting from one of the 4 directions). For the diagonal sweeps, the bar was replaced with a blank for the last 16 of the 28 steps, so that the stimuli swept diagonally across the visual field from one side to the center in twelve steps followed by 13.6 s of blanks (16 x 850 ms). Each experiment included 224 850-ms steps plus 3 s of blank at the beginning and end, for a total of 196.4 seconds.

4.5 Experimental procedure

All participants completed pRF mapping experiments in which they viewed visual stimuli for the purpose of estimating the spatial selectivity for individual electrodes (population receptive field mapping (Dumoulin &

Wandell, 2008)). In these experiments, participants were instructed to fixate on a cross located in the center of the screen and press a button every time the cross changed color (from green to red or red to green). Fixation cross color changes were created independently from the stimulus sequence and occurred at randomly chosen intervals ranging between 1 and 5 s. Participants completed one to three recording sessions. Each session included two pRF mapping experiments. The experimenter stayed in the room throughout the testing session. Participants were encouraged to take short breaks between experiments.

4.6 ECoG DATA ANALYSIS

Preprocessing

Data were preprocessed using MATLAB 2020b with custom scripts available at https://github.com/WinawerLab/ECoG_utils (see *Data and Code Availability* for access to data and computational methods to reproduce all analyses). Raw data traces obtained in each recording session were visually inspected for spiking, drift or other artifacts. Electrodes that showed large artifacts or showed epileptic activity were marked as bad and excluded from analysis. Data were then separated into individual experiments and formatted to conform to the iEEG-BIDS format (Holdgraf et al., 2019). Data for each experiment were re-referenced to the common average across electrodes for that experiment, whereby a separate common average was calculated per electrode group (i.e., separate common average for each of the 4 electrode types-standard grid, high-density grid, strip, and depth electrodes, see *bidsEcogRereference.m*). The re-referenced voltage time series for each experiment were written to BIDS derivatives directories.

Electrode localization

Intracranial electrode arrays from NYU patients were localized from the post-implantation structural T1-weighted MRI images and co-registered to the preoperative T1-weighted MRI (Yang et al., 2012). Electrodes from UMCU patients were localized from the postoperative CT scan and co-registered to the preoperative T1-weighted MRI (Hermes, Miller, Noordmans, Vansteensel, & Ramsey, 2010). Electrode coordinates were computed in native T1 space and visualized on the pial surface reconstruction of the preoperative T1-weighted scan generated using FreeSurfer.

Cortical visual field maps were generated for each individual participant based on the T1-weighted scan by aligning the surface topology with a probabilistically defined retinotopic atlas derived from a retinotopic fMRI mapping dataset as shown in **Supplementary Figure 1-1** (L. Wang, Mruczek, Arcaro, & Kastner, 2015). We use the full probability map, rather than the maximum probability map, in order to account for the uncertainty in the mapping between electrodes location and visual field map in the patient's native T1 space. For each cortical vertex, the atlas contains the probability of being assigned to each of 25 maps. Electrodes were matched to the probabilistic atlases using the following procedure (see *bidsEcogMatchElectrodesToAtlas.m* in ECoG_utils): For each electrode, the distance to all the nodes in the FreeSurfer pial surface mesh was calculated, and the node with the smallest distance was determined to be the matching node. The atlas value for the matching node was then used to assign the electrode to a probability of belonging to each of the following visual areas: V1v, V1d, V2v, V2d, V3v, V3d, hV4, VO1, VO2, PHC1, PHC2, TO2, TO1, LO2, LO1, V3b, V3a, IPS0, IPS1, IPS2, IPS3, IPS4, IPS5, SPL1, or FEF. We then merged these 25 visual areas into 12 groups: V1 (V1v + V1d), V2 (V2v + V2d), V3 (V3v + V3d), hV4, VO (VO1 + VO2), PHC (PHC1 + PHC2), TO (TO1 + TO2), LO (LO1 + LO2), V3AB (V3a + V3b), IPS (IPS0–5), SPL (SPL1), or FEF.

553 The importance of assigning electrodes to areas probabilistically is that the uncertainty of assignment is
554 reflected in the uncertainty of the estimates. Were we to uniquely assign each electrode to one area using
555 maximum probability, we would likely overstate any conclusions about differences between maps.

556 To visualize the electrodes on the cortical surface we use a modified version of the Wang et al. full probability
557 atlas. First, we select vertices that have a probability greater than 95% of not belonging to any of the
558 retinotopic regions, and labeled as "none". Next, for the remaining vertices we assigned the region with the
559 highest probability, even if the probability for not belonging to one of the retinotopic regions was higher (e.g.,
560 **Figures 1, 2, Supplementary Figures 1-1, 8-1, and 8-2**).

561 **Data epoching**

562 The preprocessed data were analyzed using custom MATLAB code
563 (https://github.com/KenYMB/ECoG_alphaPRF). First, a dataset was created by reading in the voltage time
564 courses of each experiment for each participant from the corresponding BIDS derivatives folders. To combine
565 the UMCU and NYU participants into a single dataset, the UMCU data were downsampled at 512 Hz to match
566 the sample rate of the NYU data. Visual inspection of the data indicated an obvious delay in response onset
567 for the UMCU participants relative to the NYU participants. The cause of the delay could not be tracked down
568 but it was clearly artifactual. To correct the delay, UMCU data were aligned to the NYU data based on a cross-
569 correlation on the average event-related potentials (ERPs) across all stimulus conditions from the V1 and V2
570 electrodes from three participants (1 UMCU, 2 NYU). The delay in stimulus presentation was estimated to be
571 72 ms (95% CI 63 to 85 ms by bootstrapping across a total of 18 electrode pairs), and stimulus onsets of the
572 UMCU participants were shifted accordingly (Groen et al. 2022; see also the script s_determineOnsetShift
573 UMCUvsNYU.m in https://github.com/irisgroen/temporalECoG). One NYU patient (Patient 3) had
574 inaccurate trigger onset signals for each stimulus event due to a recording malfunction. The onset timings for
575 this patient were reconstructed by using the first onset in each experiment (which were recorded correctly),
576 and then assumed to begin every 850 ms as controlled by the stimulus computer. Any small error in these
577 latency corrections should have no effect on our conclusions, as the evoked potentials were computed
578 separately for each participant, and latency of evoked response played no role in our analyess.

579 The voltage data were then epoched for all trials between [-0.2 and 0.8] seconds relative to stimulus onset
580 (see *ecog_prf_getData.m*). Baseline-correction was applied by subtracting the average pre-stimulus
581 amplitude computed in [-0.2 and 0] seconds within each trial.

582 **Electrode selection and exclusion of noisy data**

583 In two participants (10 and 11), there were high-density grids over lateral posterior cortex. All electrodes from
584 these two grids were included in the pRF analyses (described below). In addition, we also included all
585 standard grid or strip electrodes which were assigned to one of the visual areas with a minimum of 5%
586 according to the Wang et al full probability atlas. Together, this resulted in 239 high-density electrodes and
587 131 standard grid or strip electrodes. After excluding 4 electrodes due to high noise (see paragraph below),
588 the data selection resulted in a total of 366 electrodes from 9 participants. Of these 366 electrodes, 334
589 covered visual areas V1, V2, V3, hV4, VO, PHC, TO, LO, V3AB, IPS, and SPL. The other 32 electrodes
590 belonged to one of the high-density grids but could not be assigned to a particular visual area.

591 Furthermore, we excluded epochs containing voltages that were large relative to the evoked signal.
592 Specifically, for each electrode, we derived a distribution of the expected peak of the evoked signal by (1)
593 converting voltage to power (squared voltage), (2) taking the maximum power from each epoch, excluding
594 blanks, during the stimulus period (0–500 ms), and (3) fitting an inverse Gaussian distribution to these

numbers. This yields one distribution for each electrode. Next, we computed the evoked potential by averaging the voltage time series across all epochs excluding blanks, and projected this out from every epoch. Finally, from the residual time series in each epoch, we compared the maximum power to the inverse Gaussian distribution for that electrode. If that value fell in the far tail, defined as the upper 0.01% of the area under the curve, then we excluded that epoch. This resulted in the exclusion of 0.8% of epochs (3,422 out of ~430,000). Twelve electrodes showed unusually high variance across trials (over three standard deviations across electrodes) and were therefore excluded from further analysis. Furthermore, two runs from Patient 3 were not included in final analyses, as the patient broke fixation during these runs (see *ecog_prf_selectData.m*).

Computing power spectral density

We computed power spectral density (PSD) for each electrode in each epoch. We assumed in our analysis that the alpha oscillation is bandpass, centered at about 8–13 Hz, and that the biophysical processes giving rise to the oscillation are distinct from those causing the low-pass visually evoked potential. The two signals overlap in frequency, however. Hence, in order to remove the influence of the evoked signal on estimates of alpha power (and other spectral responses) (Hermes et al., 2015; Hermes et al., 2017), we computed the averaged ERPs separately for epochs with stimulus presentation and for epochs without stimuli (blanks). We then regressed the ERP time series out from each epoch (see *ecog_prf_regressData.m*). From the time series after removal of the ERP, we computed the PSD during the stimulus presentation period (0–500 ms) in 1 Hz bins. We used Welch's (1967) method with a 200 ms length Hann window with 50% overlap to attenuate edge effects. Baseline power spectra were computed for each electrode by taking a geometric average of the power spectra at each frequency bin across blank epochs (see *ecog_prf_spectra.m*).

4.7 pRF ANALYSIS

Each participant had multiple identical pRF runs, with the same sequence of 224 trials per run, and 2 to 6 runs per participant. For each electrode and for each of the 224 trials, we computed the geometric mean of the PSD per frequency bin across the repeated runs, to yield a sequence of 224 PSDs per electrode. We extracted a summary measure of alpha power and broadband power from each of the PSDs, so that for each electrode, we obtained a series of 224 alpha values and 224 broadband values.

Estimating alpha power from the PSD

We used a model-based approach to compute the alpha responses. This is important because the broadband response extends to low frequencies, and if one just measured the power in a pre-defined range of frequencies corresponding to the alpha band, it would reflect a sum of the two signals rather than the alpha response alone.

To decompose the spectral power into a broadband shift and a change in the alpha oscillation, we modeled the spectral power changes in the 3 to 26 Hz range as the sum of two responses in the log power / log frequency domain: a linear shift to capture the broadband response and a Gaussian to capture the alpha response (**Figure 11**), according to the formula based on Hermes et al. (2015) decomposition of broadband and gamma oscillations:

$$Stimulus\ evoked\ change\ in\ power = \quad Broadband\ elevation \quad + \quad Alpha\ suppression$$

$$\log_{10}\left(\frac{P_S(k)}{P_B(k)}\right) \quad = (\beta_{broadband_low} - n(k-\mu)) \ + \ \beta_{alpha}\, G(k|\mu,\sigma),$$

$$k = \log_{10}(frequency),$$

$$G(k|\mu,\sigma) = e^{\frac{-(k-\mu)^2}{2\sigma^2}},$$

with $8\ Hz < 10^{\mu} < 13\ Hz$. **[Equation 1]**

$P(k)$ is the power spectral density (PSD), either for the stimulus (P_S) or the blank (P_B). 10^{μ} indicates the peak alpha frequency. We define the change in power as the logarithm of the ratio, so that, for example, a doubling or halving in power are treated symmetrically. Typically, the response to a stimulus is an increase in broadband power and a decrease in the alpha oscillation, so $\beta_{broadband_low}$ is usually positive and β_{alpha} is usually negative. We refer to the broadband component as $\beta_{broadband_low}$ to distinguish it from the broadband power we estimate at higher frequencies (70–180 Hz). While the two responses might result from a common biological cause, as proposed by (Miller, Sorensen, et al., 2009), we treat the power elevation at lower and higher frequencies separately here. This ensures that the pRFs estimated from the broadband response (70–180 Hz) and from the alpha responses are independent measures, and that any relationship between them is not an artifact of the decomposition method. Confining the broadband signal to higher frequencies to estimate the broadband pRFs also facilitates comparison with other reports, since most groups exclude low frequencies from their estimates of ECoG broadband data. Hence the term $\beta_{broadband_low}$ is defined here only to help estimate the alpha response, and is not used directly for fitting pRF models in our main analysis comparing alpha and broadband pRFs.

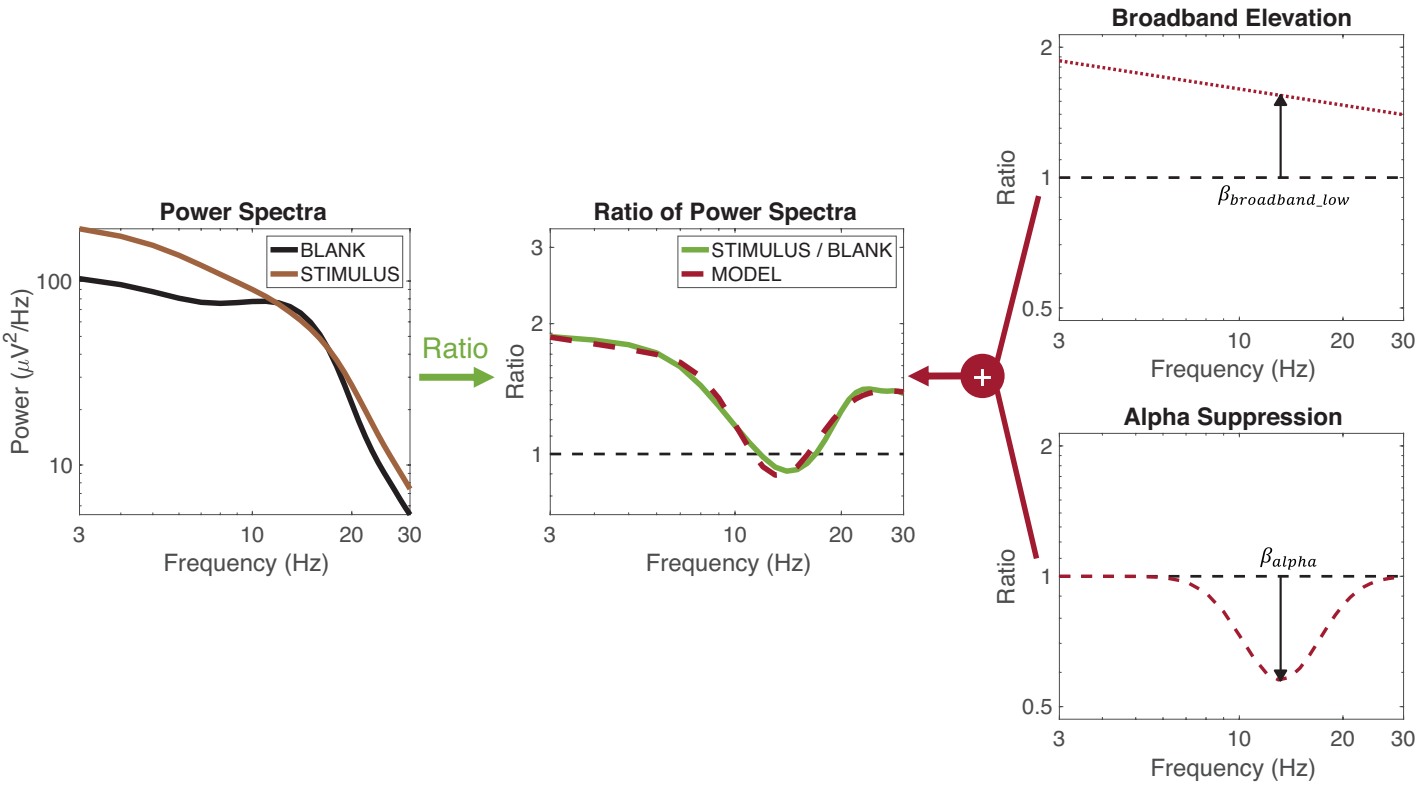

Figure 11. Schematics of model-based alpha computation. The left panel shows the average power spectra elicited by the pRF mapping stimuli (brown) and blanks (black) from a representative electrode. The middle panel shows the ratio between the two power spectra (green). This ratio, evaluated on log-log axes, is modeled (dashed red) as the sum of a broadband elevation (right panel, top) and an alpha suppression (right panel, bottom). The magnitude of alpha suppression is the coefficient of the Gaussian bump (β_{alpha}, black arrow). See **Equation 1** and *makeFigure11.m*.

For two participants, there was a prominent spectral peak just above the alpha band (~24 Hz, beta band), which interfered with this spectral decomposition. In this case, we added a third component to the model, identical to the term for alpha, except with a center constrained to 15–30 Hz instead of 8 to 13 Hz, and applied the model in the 3 to 32 Hz range:

$$\log_{10}\left(\frac{P_S(k)}{P_B(k)}\right) = (\beta_{broadband_low} - n(k-\mu_1)) + \beta_{alpha}\, G(k|\mu_1,\sigma_1) + \beta_{beta}\, G(k|\mu_2,\sigma_2),$$

$$k = \log_{10}(frequency),$$

$$G(k|\mu_1,\sigma_1) = e^{\frac{-(k-\mu_1)^2}{2\sigma_1{}^2}},\ G(k|\mu_2,\sigma_2) = e^{\frac{-(k-\mu_2)^2}{2\sigma_2{}^2}},$$

with $8\ Hz < 10^{\mu_1} < 13\ Hz$ and $15\ Hz < 10^{\mu_2} < 30\ Hz$. **[Equation 2]**

The amplitude of this beta oscillation was modeled as a nuisance variable in that it helped improve our estimate of the alpha oscillation but was not used further in analysis. Including this additional term for the other participants had negligible effect, since there were not clear beta oscillations in other participants so that the coefficient was usually close to 0. For simplicity, we omitted the beta terms for all datasets except for the two participants which required it. This spectral decomposition was computed for each aperture step in the pRF experiments with the constraint that the peak alpha frequency, 10^{μ}, was within ±1 Hz of the peak estimated from averaging across the responses to all apertures for each electrode.

Estimating broadband power from the PSD

Separately, we estimated the broadband power elevation in the higher frequency range (70–180 Hz) for each electrode and each stimulus location. The broadband power elevation was defined as the ratio of stimulus power (P_S) to blank power (P_B), where power was computed as the geometric mean across frequencies from 70 to 180 Hz in 1-Hz bins, according to the formula:

$$Broadband\ elevation = \beta_{broadband} = \frac{geometric\ mean\ (P_S(f))}{geometric\ mean\ (P_B(f))},$$

with $70\ Hz < f < 180\ Hz$ (excluding harmonics of line noise). **[Equation 3]**

The harmonics of power line components were excluded from the averaging: 116–125 and 176–180 Hz from NYU patients and 96–105 and 146–155 Hz from UMCU patients.

Time courses from pRF analyses

The computations above yield one estimate of alpha power and one estimate of broadband power per trial per electrode, meaning two time series with 224 samples. Visual inspection showed that these two metrics both tended to rise and fall relatively slowly relative to the small changes in position of the sweeping bar aperture. Therefore, the rapid fluctuations in the summary time series were mostly noise. To increase signal-to-noise ratio, each time course was decimated using a lowpass Chebyshev Type I infinite impulse response (IIR) filter of order 3, resulting in 75 time points (see *ecog_prf_fitalpha.m* and *ecog_prf_constructTimeSeries.m*). The same decimation procedure was applied to the binary contrast aperture time series.

Fitting pRF models

The alpha and broadband power time course and the sequential stimulus contrast apertures were used to estimate two pRFs per electrode (one for alpha, one for broadband), using a Difference of Gaussians (DoG) model (Zuiderbaan, Harvey, & Dumoulin, 2012). The DoG model predicts the response amplitude as the dot product of the binarized stimulus aperture and a pRF. For broadband, the pRF was assumed to be a positive 2D Gaussian (circular) summed with a negative surround. For alpha, the pRF was assumed to be negative with a positive surround. Early analyses indicated a need for the surround, but a lack of precision in estimating its size. For simplicity and to avoid overfitting, we assumed the surround to extend infinitely. Hence the pRF is a Gaussian with an offset. For each model (alpha and broadband) for each electrode, 5 parameters were fit: center location of the pRF (x, y), standard deviation of the center Gaussian (σ), and the gains of the center (g_1) and the surround (g_2). We estimated these pRF parameters using the analyzePRF toolbox (Kay, Winawer, Mezer, et al., 2013). We modified the toolbox to incorporate the surround (see *analyzePRFdog.m* in ECoG_utils). The predicted response is obtained by the dot product of aperture and pRF:

$$RESP = STIM \cdot PRF,$$

$$RESP = STIM \cdot (g_1 \cdot G_1(x, y, \sigma) - g_2).$$

[Equation 4]

We optimized the parameters $(x, y, \sigma, g_1, and\ g_2)$ across all stimulus locations by maximizing the coefficient of determination (R^2) between the 75 predicted time points and observed time series using a least squares non-linear search solver (*lsqcurvefit*), employing the levenberg-marquardt algorithm:

$$R^2 = 1 - \frac{\sum_{stimuli}(RESP_{MODEL} - RESP_{DATA})^2}{\sum_{stimuli} RESP_{DATA}{}^2}.$$

[Equation 5]

We set the boundary on the center of Gaussian (x, y) as [-16.6° and 16.6°], two times the maximal extent of the visual stimulus. We performed the fitting twice, once to compute pRF parameters and once to compute model accuracy separately. We use the results of the fit to the complete dataset for each electrode to report pRF parameters. To estimate model accuracy, we fit the data using two-fold cross-validation. For cross-validation, each time course was separated into first and second half time courses. Both halves included all horizontal and vertical stimulus positions but reversed in temporal order. We estimated the pRF parameters from each half time course (37 or 38 time points), and used these parameters to predict the response to the other half of the time course. Then we obtained the cross-validated coefficient of determination as the model accuracy of the concatenated predictions (R^2):

$$cross\text{-}validated\ R^2 = 1 - \frac{\sum(RESP_{cross\text{-}validated\ MODEL} - RESP_{DATA})^2}{\sum RESP_{DATA}{}^2}.$$

[Equation 6]

To summarize the data from each electrode, we took the cross-validated variance explained from the split half analysis, and the parameter estimates from the full fit, converting the x and y parameters to polar angle and eccentricity (see *ecog_prf_analyzePRF.m*).

722 **Comparison of alpha and broadband pRFs**

723 We compared the pRF parameters for the alpha model and broadband models for a subset of electrodes
724 which showed reasonably good fits for each of the two measures. To be included in the comparison,
725 electrodes needed to have a pRF center within the maximal stimulus extent (8.3°) for both broadband and
726 alpha, and to have a goodness of fit exceeding thresholds for both broadband and alpha.

727 The goodness of fit thresholds were defined based on null distributions. The null distributions were
728 computed separately for broadband and alpha. In each case, we shuffled the assignment of pRF parameters
729 to electrodes, computing how accurately the pRF model from one electrode explained the time series from a
730 different electrode. We did this 5,000 times to compute a distribution, and chose a variance explained
731 threshold that was higher than 95% of the values in this null distribution. That value was 31% for broadband
732 and 22% for alpha (**Supplementary Figure 4-1**). Electrodes whose cross-validated variance explained
733 without shuffling exceeded these values were included for the comparison between the two types of signals
734 (assuming their pRF centers were within the 8.3° stimulus aperture).

735 This procedure resulted in 54 electrodes from 4 patients. Of these, 35 electrodes had non-zero probability
736 assignments to V1, V2, or V3, 45 to dorsolateral visual areas (TO, LO, V3AB, or IPS), and 3 to ventral visual
737 areas (hV4, VO, or PHC). The total is greater than 54 because of the probabilistic assignment of electrodes to
738 areas (See *Electrode localization* for the probabilistic assignment). See **Table 2** for details.

	Visual area	**# of electrodes with probability > 0**	**Contributing patients (# of electrodes)**
Electrodes in visual areas (Figures 3-S1, 4-S1)	V1–V3	104	1 (1), 2 (15), 3 (6), 4 (13), 5 (6), 8 (54), 9 (9)
	Dorsolateral	303	1 (7), 2 (7), 3 (18), 4 (19), 5 (18), 6 (6), 7 (8), 8 (130), 9 (90)
	V1–V3 or dorsolateral	329	1 (7), 2 (19), 3 (21), 4 (28), 5 (20), 6 (6), 7 (8), 8 (130), 9 (90)
Electrodes with broadband pRFs (Figures 4, 4-S2, 7, 7-S1)	V1–V3	55	1 (1), 2 (9), 5 (6), 8 (32), 9 (7)
	Dorsolateral	121	1 (1), 2 (2), 3 (1), 4 (1), 5 (4), 7 (1), 8 (63), 9 (48)
	V1–V3 or dorsolateral	131	1 (1), 2 (10), 3 (1), 4 (1), 5 (6), 7 (1), 8 (63), 9 (48)
Electrodes with broadband and alpha pRFs (Figures 1-S2, 3, 5, 5-S1, 5-S2, 6, 6-S1, 6-S2)	V1–V3	35	2 (6), 5 (5), 8 (20), 9 (4)
	Dorsolateral	45	5 (3), 8 (25), 9 (17)
	V1–V3 or dorsolateral	53	2 (6), 5 (5), 8 (25), 9 (17)

Table 2. Overview of electrodes and patients per visual area and figure. *Electrodes in visual areas* (rows 1-3) indicate electrodes with > 0% probability of being in an either V1 to V3 or dorsolateral maps, irrespective of the accuracy of pRF fits. *Electrodes with broadband pRFs* (rows 4-6) indicate the subset of electrodes from rows 1-3 exceeding a threshold variance explained by the broadband pRF model. *Electrodes with broadband and alpha pRFs* (rows 7-9) are the subset of electrodes from rows 4-6 satisfying selection criteria both for broadband and alpha pRFs (exceeding threshold variance explained and a pRF center within the stimulus aperture). The totals for rows "V1–V3 or dorsolateral" are greater than the sum of "V1-V3" and "dorsolateral" because some electrodes have greater than 0% probability of being included in both groups (see *Electrode Localization*, section 4.6). Any electrode with greater than 95% chance of being assigned to no visual area in the atlas was excluded from the table entirely.

To summarize the relationship between broadband and alpha pRF parameters separately for low (V1–V3) vs. high (dorsolateral) visual areas, we used a resampling procedure that accounts for uncertainty of the assignment between electrodes and visual area. We sampled from the 54 electrodes 54 times with replacement, and randomly assigned each electrode to a visual area according to the Wang full probability distributions. After the resampling, on average, 17.7 electrodes were assigned to V1–V3, 23.2 to dorsolateral, and 12.1 to neither. The reason for the "neither" assignments is that the total probability (100%) of each electrode is the sum of probability of V1-V3, probability of dorsolateral, and probability of elsewhere in the brain. We repeated this procedure 5,000 times. We then plotted pRF parameters from the broadband and alpha models as 2D histograms (e.g., **Figure 5**, **Supplementary Figures 5-1, and 6-2**). For the 2D histograms, we computed and plotted 68% confidence intervals derived from the covariance matrix using the function *error_ellipse.m* (https://www.mathworks.com/matlabcentral/fileexchange/4705-error_ellipse).

4.8 Coherence analysis

Coherence in the high-density grids

We assessed the spatial dependence of coherence in each of the two signals (broadband and alpha) by analyzing data from the two high-density grids (Patients 8 and 9). For each pair of electrodes on a grid, we computed the cross power spectral density (CPSD) in each epoch. The CPSD was computed on the time series after regressing out the ERPs, as described above (*Computing power spectral density*) in 500-ms sliding windows (75% overlap, Hann windows, Welch's method (1967)). Regressing out the ERPs ensures that coherence measured between electrodes is not a result of the two electrodes having similar stimulus-triggered responses. The CPSD was calculated over the stimulus interval (-200–800 ms) in 1 Hz frequency bins (see *ecog_prf_crossspectra.m*). For each electrode pair, and for each of the 224 time series, the magnitude-squared coherence (MSC) was computed and averaged across the *N* repeated experiments:

$$MSC_{xy}(f) = \frac{1}{N}\sum_{runs}^{N} \frac{P_{xy}(f)\, P_{xy}^{*}(f)}{P_x(f)\, P_y(f)},$$

where P_{xy} is the CPSD across two electrodes, and P_x, P_y are the PSDs at each electrode. **[Equation 7]**

This calculation returns an array of time series by frequency bins for each electrode pair (see *ecog_prf_connectivity.m*). We defined the alpha coherence between a seed electrode and all other electrodes on the high-density grid as the coherence at the peak alpha frequency. We defined broadband coherence as the average of the coherence in the broadband frequency range, 70–180 Hz. For every electrode pair on a grid, we then had 224 measures of alpha coherence and 224 measures of broadband coherence. For consistency with the pRF analyses, these time series of alpha and broadband coherence were again decimated into 75 time points.

We then binned the coherence data by electrode pair as a function of inter-electrode distance and by trial as a function of stimulus location. Electrode pairs were binned into inter-electrode distances in multiples of 3 mm. Only electrodes pairs for which the seed electrode satisfied the pRF threshold as computed in the previous section were selected (see *Comparison of alpha and broadband pRFs*). We used bootstrapping to compute error bars. For each inter-electrode distance, we randomly sampled electrode pairs with replacement, and averaged the coherence across the electrode pairs and trials. We repeated this procedure 5,000 times. The averaged coherences were fitted to the exponential decay function across inter-electrode distances using the least squares method.

ACKNOWLEDGMENTS

We thank **Dora Hermes** (Mayo Clinic) for help on the model-based method to analyze alpha oscillations, and for feedback on an earlier version of the work; **Mike Landy** (NYU) for suggesting we compare the spatial spread of attentional cueing with the spatial spread of the alpha pRF; **Kaoru Amano** (U Tokyo) and his lab for providing feedback on an early version of the work; **Ilona Bloem** (NYU) for feedback on the manuscript; and **Hiromasa Takemura** (NIPS, Japan) for providing feedback on the project. This work was supported in part through the NYU IT High Performance Computing resources, services, and staff expertise.

REFERENCES

Adrian, E. D., & Matthews, B. H. C. (1934). The Berger rhythm potential changes from the occipital lobes in man. *Brain, 57*(4), 355-385.

Bair, W., Cavanaugh, J. R., & Movshon, J. A. (2003). Time course and time-distance relationships for surround suppression in macaque V1 neurons. *J Neurosci, 23*(20), 7690-7701.

Barry, R. J., Clarke, A. R., Johnstone, S. J., Magee, C. A., & Rushby, J. A. (2007). EEG differences between eyes-closed and eyes-open resting conditions. *Clin Neurophysiol, 118*(12), 2765-2773.

Bartoli, E., Bosking, W., Chen, Y., Li, Y., Sheth, S. A., Beauchamp, M. S., et al. (2019). Functionally Distinct Gamma Range Activity Revealed by Stimulus Tuning in Human Visual Cortex. *Curr Biol, 29*(20), 3345-3358 e3347.

Bastos, A. M., Lundqvist, M., Waite, A. S., Kopell, N., & Miller, E. K. (2020). Layer and rhythm specificity for predictive routing. *Proc Natl Acad Sci U S A, 117*(49), 31459-31469.

Bedard, C., Kroger, H., & Destexhe, A. (2006). Does the 1/f frequency scaling of brain signals reflect self-organized critical states? *Phys Rev Lett, 97*(11), 118102.

Berger, H. (1929). Über das Elektrenkephalogramm des Menschen. *Archiv für Psychiatrie und Nervenkrankheiten, 87*(1), 527-570.

Bollimunta, A., Mo, J., Schroeder, C. E., & Ding, M. (2011). Neuronal mechanisms and attentional modulation of corticothalamic alpha oscillations. *J Neurosci, 31*(13), 4935-4943.

Brovelli, A., Lachaux, J. P., Kahane, P., & Boussaoud, D. (2005). High gamma frequency oscillatory activity dissociates attention from intention in the human premotor cortex. *Neuroimage, 28*(1), 154-164.

Busch, N. A., Dubois, J., & VanRullen, R. (2009). The phase of ongoing EEG oscillations predicts visual perception. *J Neurosci, 29*(24), 7869-7876.

Canolty, R. T., Edwards, E., Dalal, S. S., Soltani, M., Nagarajan, S. S., Kirsch, H. E., et al. (2006). High gamma power is phase-locked to theta oscillations in human neocortex. *Science, 313*(5793), 1626-1628.

Carrasco, M. (2011). Visual attention: the past 25 years. *Vision Res, 51*(13), 1484-1525.

Clayton, M. S., Yeung, N., & Cohen Kadosh, R. (2018). The many characters of visual alpha oscillations. *Eur J Neurosci, 48*(7), 2498-2508.

Crone, N. E., Miglioretti, D. L., Gordon, B., & Lesser, R. P. (1998). Functional mapping of human sensorimotor cortex with electrocorticographic spectral analysis. II. Event-related synchronization in the gamma band. *Brain, 121 (Pt 12)*, 2301-2315.

Donoghue, T., Haller, M., Peterson, E. J., Varma, P., Sebastian, P., Gao, R., et al. (2020). Parameterizing neural power spectra into periodic and aperiodic components. *Nat Neurosci, 23*(12), 1655-1665.

Downing, C. J., & Pinker, S. (1985). The spatial structure of visual attention. In *Mechanisms of attention: Attention and performance XI* (pp. 171-187).

Drewes, J., & VanRullen, R. (2011). This is the rhythm of your eyes: the phase of ongoing electroencephalogram oscillations modulates saccadic reaction time. *J Neurosci, 31*(12), 4698-4708.

Dugue, L., Merriam, E. P., Heeger, D. J., & Carrasco, M. (2020). Differential impact of endogenous and exogenous attention on activity in human visual cortex. *Sci Rep, 10*(1), 21274.

Dumoulin, S. O., & Wandell, B. A. (2008). Population receptive field estimates in human visual cortex. *Neuroimage, 39*(2), 647-660.

Eckhorn, R., Bauer, R., Jordan, W., Brosch, M., Kruse, W., Munk, M., et al. (1988). Coherent oscillations: a mechanism of feature linking in the visual cortex? Multiple electrode and correlation analyses in the cat. *Biol Cybern, 60*(2), 121-130.

Foster, J. J., Sutterer, D. W., Serences, J. T., Vogel, E. K., & Awh, E. (2017). Alpha-Band Oscillations Enable Spatially and Temporally Resolved Tracking of Covert Spatial Attention. *Psychol Sci, 28*(7), 929-941.

Gray, C. M., & Singer, W. (1989). Stimulus-specific neuronal oscillations in orientation columns of cat visual cortex. *Proc Natl Acad Sci U S A, 86*(5), 1698-1702.

Groen, I. I. A., Piantoni, G., Montenegro, S., Flinker, A., Devore, S., Devinsky, O., et al. (2022). Temporal Dynamics of Neural Responses in Human Visual Cortex. *J Neurosci, 42*(40), 7562-7580.

Harvey, B. M., Vansteensel, M. J., Ferrier, C. H., Petridou, N., Zuiderbaan, W., Aarnoutse, E. J., et al. (2013). Frequency specific spatial interactions in human electrocorticography: V1 alpha oscillations reflect surround suppression. *Neuroimage, 65*, 424-432.

Hermes, D., Miller, K. J., Noordmans, H. J., Vansteensel, M. J., & Ramsey, N. F. (2010). Automated electrocorticographic electrode localization on individually rendered brain surfaces. *J Neurosci Methods, 185*(2), 293-298.

Hermes, D., Miller, K. J., Wandell, B. A., & Winawer, J. (2015). Stimulus Dependence of Gamma Oscillations in Human Visual Cortex. *Cereb Cortex, 25*(9), 2951-2959.

Hermes, D., Nguyen, M., & Winawer, J. (2017). Neuronal synchrony and the relation between the blood-oxygen-level dependent response and the local field potential. *PLoS Biol, 15*(7), e2001461.

Hermes, D., Petridou, N., Kay, K. N., & Winawer, J. (2019). An image-computable model for the stimulus selectivity of gamma oscillations. *Elife, 8*, 583567.

Holdgraf, C., Appelhoff, S., Bickel, S., Bouchard, K., D'Ambrosio, S., David, O., et al. (2019). iEEG-BIDS, extending the Brain Imaging Data Structure specification to human intracranial electrophysiology. *Sci Data, 6*(1), 102.

Hughes, S. W., & Crunelli, V. (2007). Just a phase they're going through: the complex interaction of intrinsic high-threshold bursting and gap junctions in the generation of thalamic alpha and theta rhythms. *Int J Psychophysiol, 64*(1), 3-17.

Hughes, S. W., Lorincz, M. L., Blethyn, K., Kekesi, K. A., Juhasz, G., Turmaine, M., et al. (2011). Thalamic Gap Junctions Control Local Neuronal Synchrony and Influence Macroscopic Oscillation Amplitude during EEG Alpha Rhythms. *Front Psychol, 2*, 193.

Jensen, O., & Mazaheri, A. (2010). Shaping functional architecture by oscillatory alpha activity: gating by inhibition. *Front Hum Neurosci, 4*, 186.

Kay, K. N., Winawer, J., Mezer, A., & Wandell, B. A. (2013). Compressive spatial summation in human visual cortex. *J Neurophysiol, 110*(2), 481-494.

Kay, K. N., Winawer, J., Rokem, A., Mezer, A., & Wandell, B. A. (2013). A two-stage cascade model of BOLD responses in human visual cortex. *PLoS Comput Biol, 9*(5), e1003079.
Kelly, S. P., Lalor, E. C., Reilly, R. B., & Foxe, J. J. (2006). Increases in alpha oscillatory power reflect an active retinotopic mechanism for distracter suppression during sustained visuospatial attention. *J Neurophysiol, 95*(6), 3844-3851.
Klimesch, W., Doppelmayr, M., Russegger, H., Pachinger, T., & Schwaiger, J. (1998). Induced alpha band power changes in the human EEG and attention. *Neurosci Lett, 244*(2), 73-76.
Klimesch, W., Sauseng, P., & Hanslmayr, S. (2007). EEG alpha oscillations: the inhibition-timing hypothesis. *Brain Res Rev, 53*(1), 63-88.
Klink, P. C., Chen, X., Vanduffel, W., & Roelfsema, P. R. (2021). Population receptive fields in nonhuman primates from whole-brain fMRI and large-scale neurophysiology in visual cortex. *Elife, 10*.
Kupers, E. R., Wang, H. X., Amano, K., Kay, K. N., Heeger, D. J., & Winawer, J. (2018). A non-invasive, quantitative study of broadband spectral responses in human visual cortex. *PLoS One, 13*(3), e0193107.
Le, R., Witthoft, N., Ben-Shachar, M., & Wandell, B. (2017). The field of view available to the ventral occipito-temporal reading circuitry. *J Vis, 17*(4), 6.
Lerma-Usabiaga, G., Benson, N., Winawer, J., & Wandell, B. A. (2020). A validation framework for neuroimaging software: The case of population receptive fields. *PLoS Comput Biol, 16*(6), e1007924.
Lorincz, M. L., Kekesi, K. A., Juhasz, G., Crunelli, V., & Hughes, S. W. (2009). Temporal framing of thalamic relay-mode firing by phasic inhibition during the alpha rhythm. *Neuron, 63*(5), 683-696.
Luo, L., Wang, X., Lu, J., Chen, G., Luan, G., Li, W., et al. (2023). Local field potentials, spiking activity, and receptive fields in human visual cortex. *Sci China Life Sci*.
Makeig, S. (1993). Auditory event-related dynamics of the EEG spectrum and effects of exposure to tones. *Electroencephalogr Clin Neurophysiol, 86*(4), 283-293.
Manning, J. R., Jacobs, J., Fried, I., & Kahana, M. J. (2009). Broadband shifts in local field potential power spectra are correlated with single-neuron spiking in humans. *J Neurosci, 29*(43), 13613-13620.
Mathewson, K. E., Gratton, G., Fabiani, M., Beck, D. M., & Ro, T. (2009). To see or not to see: prestimulus alpha phase predicts visual awareness. *J Neurosci, 29*(9), 2725-2732.
Matousek, M., & Petersen, I. (1983). A method for assessing alertness fluctuations from EEG spectra. *Electroencephalogr Clin Neurophysiol, 55*(1), 108-113.
Mazaheri, A., & Jensen, O. (2010). Rhythmic pulsing: linking ongoing brain activity with evoked responses. *Front Hum Neurosci, 4*, 177.
Miller, K. J., Honey, C. J., Hermes, D., Rao, R. P., denNijs, M., & Ojemann, J. G. (2014). Broadband changes in the cortical surface potential track activation of functionally diverse neuronal populations. *Neuroimage, 85 Pt 2*(0 2), 711-720.
Miller, K. J., Sorensen, L. B., Ojemann, J. G., & den Nijs, M. (2009). Power-law scaling in the brain surface electric potential. *PLoS Comput Biol, 5*(12), e1000609.
Miller, K. J., Zanos, S., Fetz, E. E., den Nijs, M., & Ojemann, J. G. (2009). Decoupling the cortical power spectrum reveals real-time representation of individual finger movements in humans. *J Neurosci, 29*(10), 3132-3137.
Moore, T., & Fallah, M. (2001). Control of eye movements and spatial attention. *Proc Natl Acad Sci U S A, 98*(3), 1273-1276.
Nakayama, K., & Mackeben, M. (1989). Sustained and transient components of focal visual attention. *Vision Res, 29*(11), 1631-1647.
Newsome, W. T., Maunsell, J. H., & Van Essen, D. C. (1986). Ventral posterior visual area of the macaque: visual topography and areal boundaries. *J Comp Neurol, 252*(2), 139-153.
Oostenveld, R., Fries, P., Maris, E., & Schoffelen, J. M. (2011). FieldTrip: Open source software for advanced analysis of MEG, EEG, and invasive electrophysiological data. *Comput Intell Neurosci, 2011*, 156869.
Osipova, D., Hermes, D., & Jensen, O. (2008). Gamma power is phase-locked to posterior alpha activity. *PLoS One, 3*(12), e3990.
Palva, S., & Palva, J. M. (2011). Functional roles of alpha-band phase synchronization in local and large-scale cortical networks. *Front Psychol, 2*, 204.
Palva, S., & Palva, J. M. (2012). Discovering oscillatory interaction networks with M/EEG: challenges and breakthroughs. *Trends Cogn Sci, 16*(4), 219-230.
Popov, T., Gips, B., Kastner, S., & Jensen, O. (2019). Spatial specificity of alpha oscillations in the human visual system. *Hum Brain Mapp, 40*(15), 4432-4440.
Popov, T., Langer, N., Gips, B., Weisz, N., & Jensen, O. (2021). Sound-location specific alpha power modulation in the visual cortex in absence of visual input. *bioRxiv*, 2021.2003.2015.435371.
Popov, T., Miller, G. A., Rockstroh, B., Jensen, O., & Langer, N. (2021). Alpha oscillations link action to cognition: An oculomotor account of the brain's dominant rhythm. *bioRxiv*, 2021.2009.2024.461634.
Ray, S., & Maunsell, J. H. (2011). Different origins of gamma rhythm and high-gamma activity in macaque visual cortex. *PLoS Biol, 9*(4), e1000610.
Ray, S., Ni, A. M., & Maunsell, J. H. (2013). Strength of gamma rhythm depends on normalization. *PLoS Biol, 11*(2), e1001477.
Rihs, T. A., Michel, C. M., & Thut, G. (2007). Mechanisms of selective inhibition in visual spatial attention are indexed by alpha-band EEG synchronization. *Eur J Neurosci, 25*(2), 603-610.
Samaha, J., Sprague, T. C., & Postle, B. R. (2016). Decoding and Reconstructing the Focus of Spatial Attention from the Topography of Alpha-band Oscillations. *J Cogn Neurosci, 28*(8), 1090-1097.
Sauseng, P., Klimesch, W., Stadler, W., Schabus, M., Doppelmayr, M., Hanslmayr, S., et al. (2005). A shift of visual spatial attention is selectively associated with human EEG alpha activity. *Eur J Neurosci, 22*(11), 2917-2926.
Shepherd, M., Findlay, J. M., & Hockey, R. J. (1986). The relationship between eye movements and spatial attention. *Q J Exp Psychol A, 38*(3), 475-491.
Shulman, G. L., Sheehy, J. B., & Wilson, J. (1986). Gradients of spatial attention. *Acta Psychol (Amst), 61*(2), 167-181.

Somers, D. C., Dale, A. M., Seiffert, A. E., & Tootell, R. B. (1999). Functional MRI reveals spatially specific attentional modulation in human primary visual cortex. *Proc Natl Acad Sci U S A, 96*(4), 1663-1668.
Spaak, E., de Lange, F. P., & Jensen, O. (2014). Local entrainment of alpha oscillations by visual stimuli causes cyclic modulation of perception. *J Neurosci, 34*(10), 3536-3544.
Staudigl, T., Hartl, E., Noachtar, S., Doeller, C. F., & Jensen, O. (2017). Saccades are phase-locked to alpha oscillations in the occipital and medial temporal lobe during successful memory encoding. *PLoS Biol, 15*(12), e2003404.
Takaura, K., Tsuchiya, N., & Fujii, N. (2016). Frequency-dependent spatiotemporal profiles of visual responses recorded with subdural ECoG electrodes in awake monkeys: Differences between high- and low-frequency activity. *Neuroimage, 124*(Pt A), 557-572.
Van Diepen, R. M., Foxe, J. J., & Mazaheri, A. (2019). The functional role of alpha-band activity in attentional processing: the current zeitgeist and future outlook. *Curr Opin Psychol, 29*, 229-238.
Wang, F., Chen, M., Yan, Y., Zhaoping, L., & Li, W. (2015). Modulation of Neuronal Responses by Exogenous Attention in Macaque Primary Visual Cortex. *J Neurosci, 35*(39), 13419-13429.
Wang, L., Mruczek, R. E., Arcaro, M. J., & Kastner, S. (2015). Probabilistic Maps of Visual Topography in Human Cortex. *Cereb Cortex, 25*(10), 3911-3931.
Welch, P. (1967). The use of fast Fourier transform for the estimation of power spectra: A method based on time averaging over short, modified periodograms. *IEEE Transactions on Audio and Electroacoustics, 15*(2), 70-73.
Winawer, J., Kay, K. N., Foster, B. L., Rauschecker, A. M., Parvizi, J., & Wandell, B. A. (2013). Asynchronous broadband signals are the principal source of the BOLD response in human visual cortex. *Curr Biol, 23*(13), 1145-1153.
Worden, M. S., Foxe, J. J., Wang, N., & Simpson, G. V. (2000). Anticipatory biasing of visuospatial attention indexed by retinotopically specific alpha-band electroencephalography increases over occipital cortex. *J Neurosci, 20*(6), RC63.
Yang, A. I., Wang, X., Doyle, W. K., Halgren, E., Carlson, C., Belcher, T. L., et al. (2012). Localization of dense intracranial electrode arrays using magnetic resonance imaging. *Neuroimage, 63*(1), 157-165.
Zuiderbaan, W., Harvey, B. M., & Dumoulin, S. O. (2012). Modeling center-surround configurations in population receptive fields using fMRI. *J Vis, 12*(3), 10.

SUPPLEMENTARY DATA

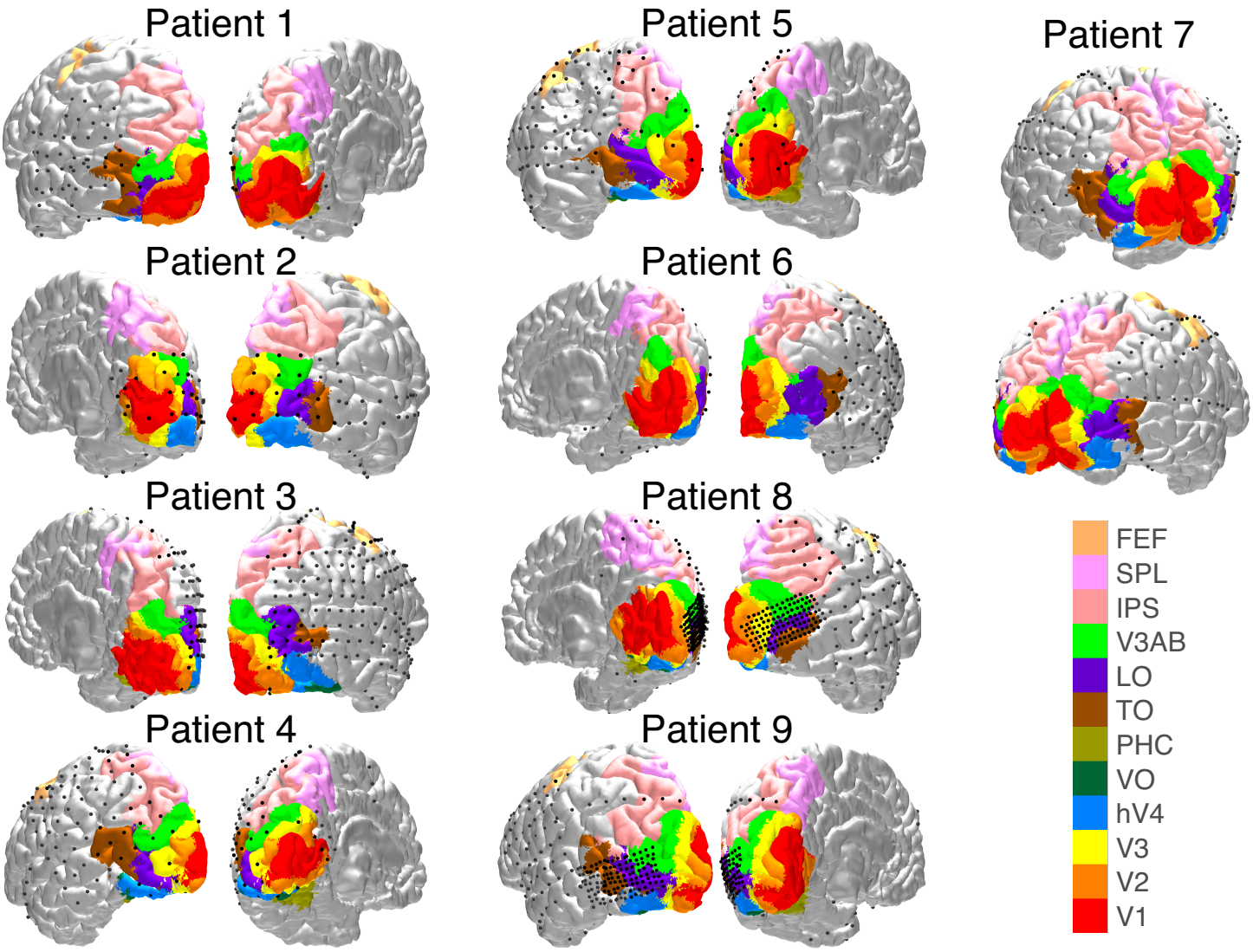

Supplementary Figure 1-1. Electrode locations and visual areas. The electrode locations and visual areas on brain surfaces for each patient. The retinotopic atlas is modified from Wang et al. (2015). Only the cortices with electrodes are shown: left cortex for Patient 1, 4, 5, and 9; right cortex for Patient 2, 3, 6, and 8; both cortices for Patient 7. See *makeFigure1S1.m*

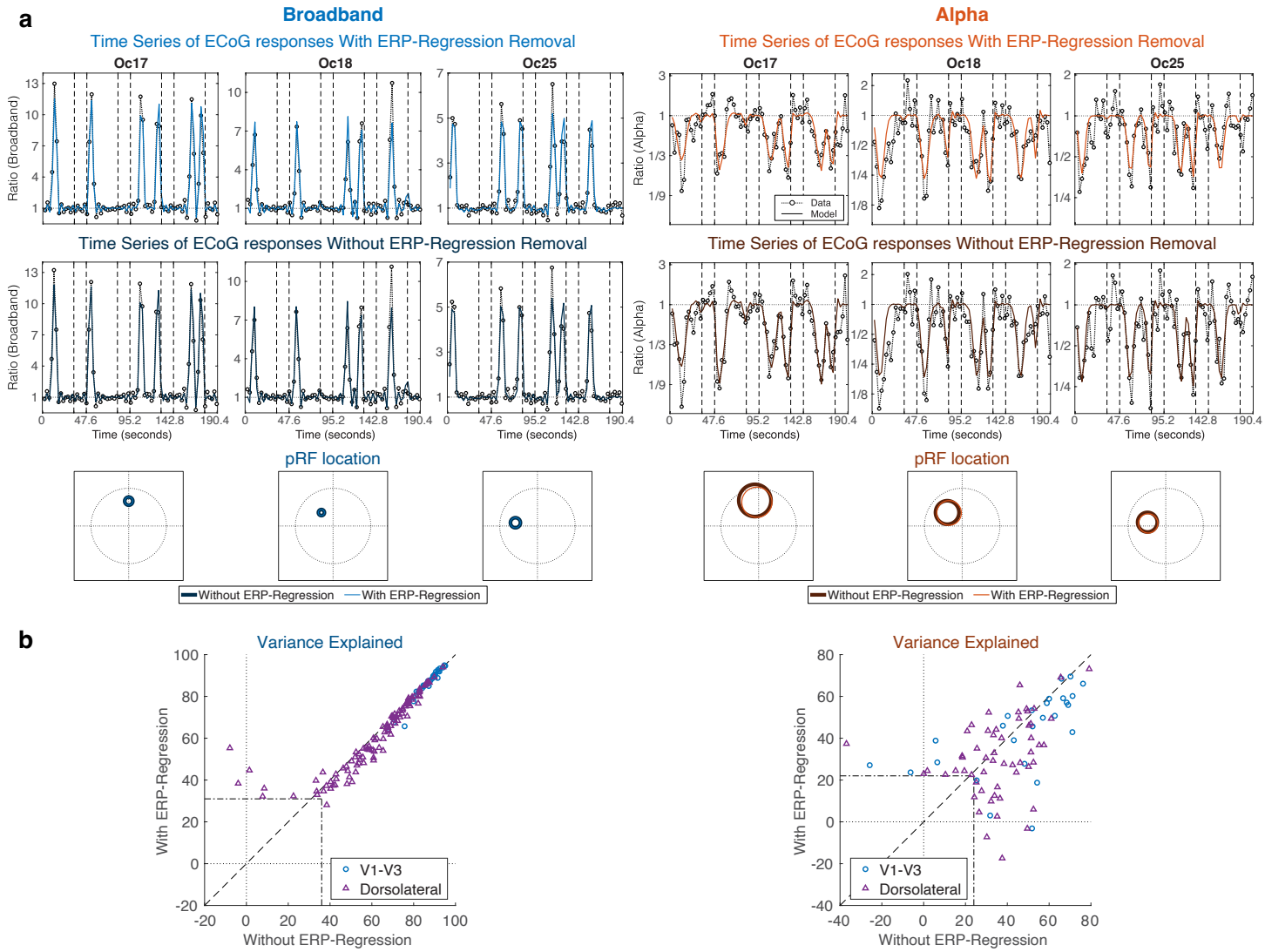

Supplementary Figure 1-2. pRF model comparisons with and without ERP-Regression Removal. (**a**) The broadband and alpha response amplitudes, along with the estimated pRF locations, are shown for three representative electrodes depicted in **Figures 1 and 2**. These summary metrics are little affected by ERP regression. (**b**) Except for a handful of electrodes in Dorsolateral maps, the cross-validated variance explained in the pRF models is nearly identical for broadband with vs without ERP regression. When the regression has a large impact, it tends to increase variance explained. There is a larger effect of ERP regression on the alpha pRF, but on average, the variance explained is the same without vs without regression. See *makeFigure1S2.m*

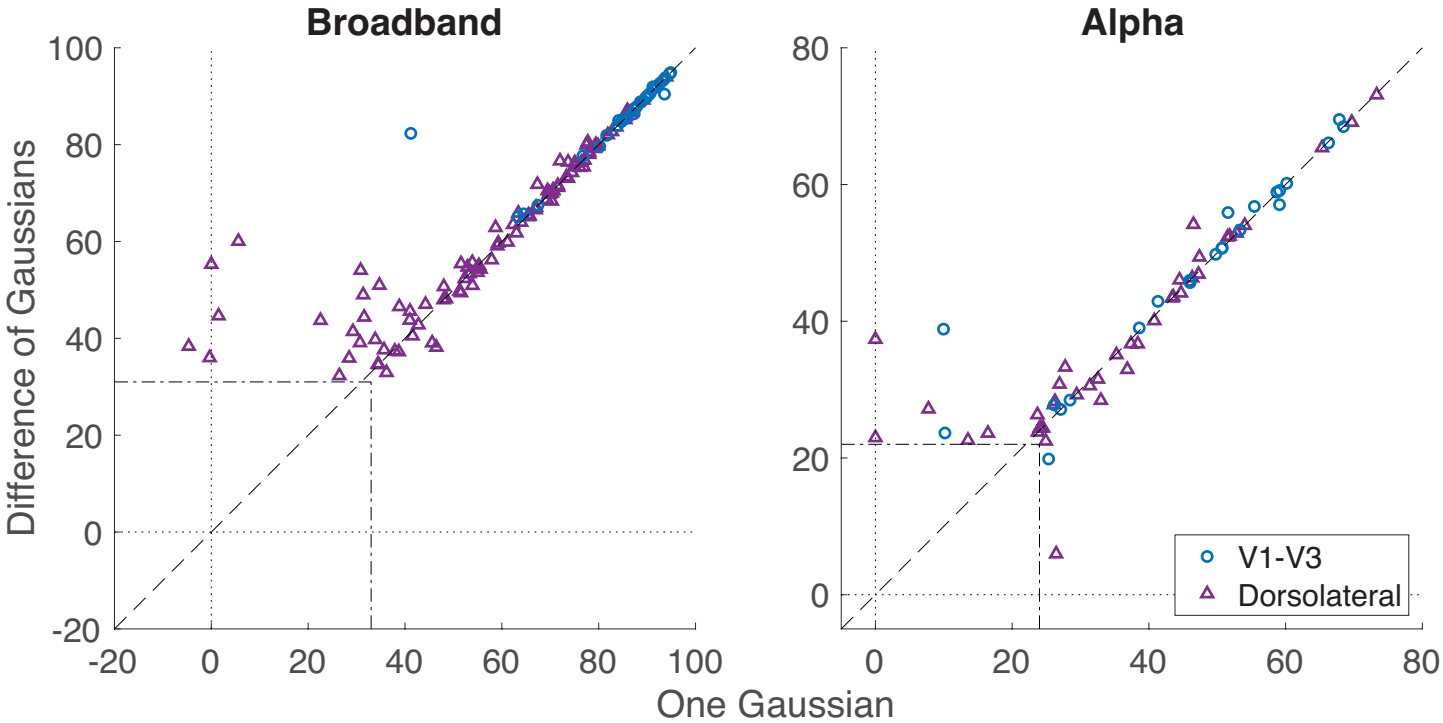

Supplementary Figure 3-1. PRF model comparisons between two Gaussian models. Cross-validated variance explained in pRF models are almost the same between two Gaussian models (Difference of Gaussians VS One Gaussian) both in V1–V3 (blue circle) and dorsolateral (purple triangle), but the Difference of Gaussians shows advantage in some electrodes. Each dot indicates electrode which is randomly selected according to the visual area probabilities in 5,000 bootstraps. See *makeFigure3S1.m*

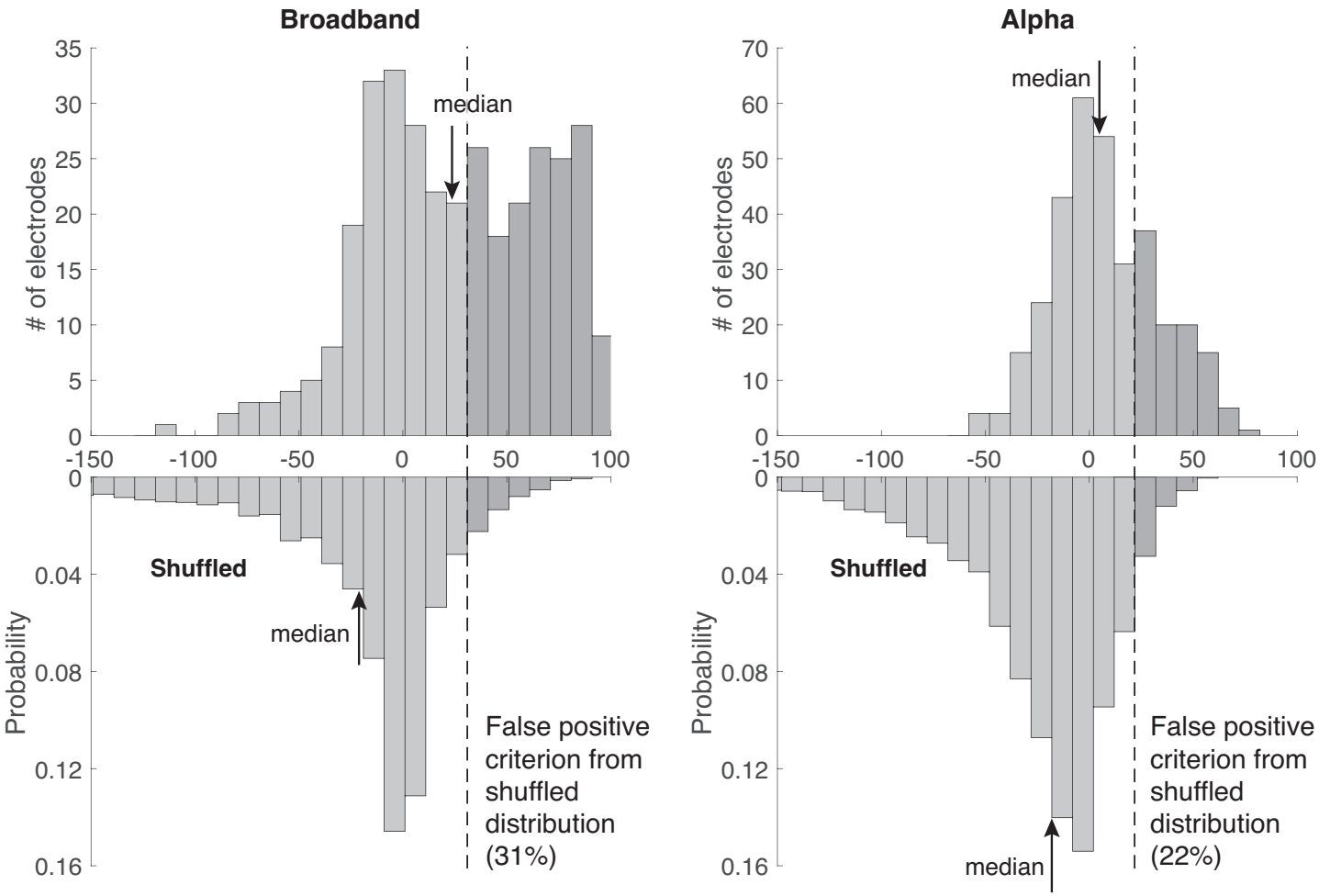

Supplementary Figure 4-1. Distributions of Variance Explained in alpha and broadband pRFs. The distributions of variance explained in alpha and broadband pRFs from all visual areas show rightward tendency compared to shuffled distributions. (A negative variance explained is common for cross-validation when making predictions with an inappropriate model.) The medians shown as black arrows have larger values in the raw distributions than the shuffled distributions (24% vs -21% in broadband and 5% vs -18% in alpha), suggesting the prediction accuracy of the pRF model fit is meaningful both in broadband and alpha. The false positive criterions were set at 95% of the values in this null distribution (dashed line: 31% for broadband and 22% for alpha). The electrodes shown in the right side of the false positive criterion (dark gray bars) were included for the comparison between broadband and alpha pRFs. in broadband pRFs are the visually selected electrodes. The electrodes shown in the right side of the false positive criterion in alpha pRFs are considered as the alpha sensitive electrodes. See *makeFigure4_4S1_4S2.m*.

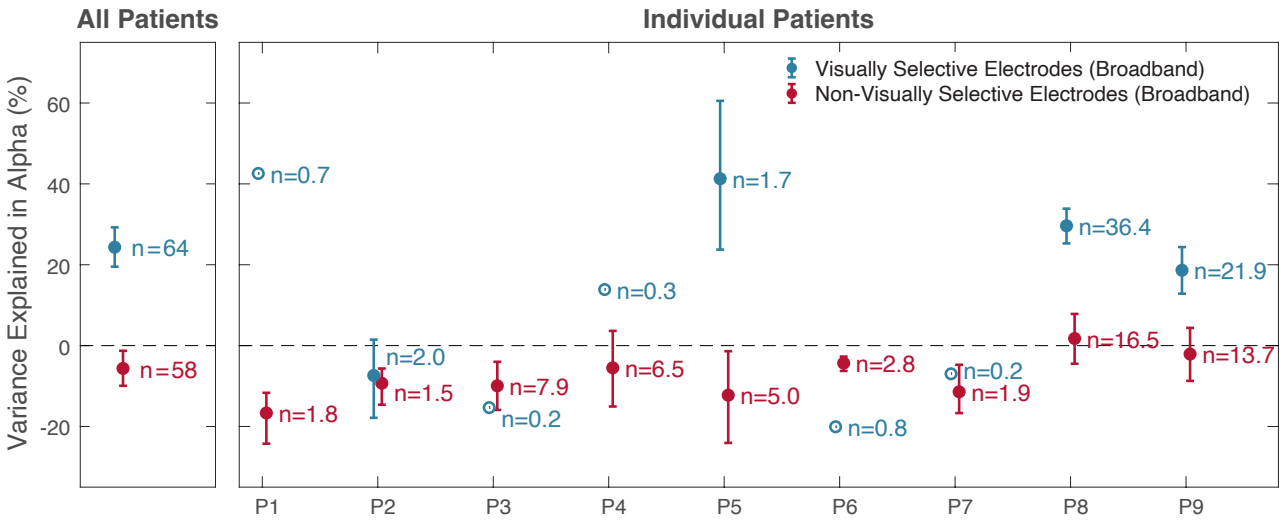

Supplementary Figure 4-2. Prediction accuracy of alpha pRF model in dorsolateral. The average two-fold cross-validated variance explained by alpha pRF models was higher in the visually selective (blue) than in the non-selective electrodes (red) except for individual patients with only 1 to 2 visually selective electrodes. The left side of the plot shows the results pooled across all patients. The right side shows the results from each patient separately. Visually selective electrodes were defined as those whose broadband pRF model accurately predicted the broadband time course. Dorsolateral includes the V3A/B, LO-1/2, TO-1/2, and IPS maps. were assigned to visual field maps probabilistically across 5,000 samples. Data points and error bars represent means ±1 standard deviation of the mean across the 5000 samples. Open dots include only one electrode each. See *makeFigure4_4S1_4S2.m*.

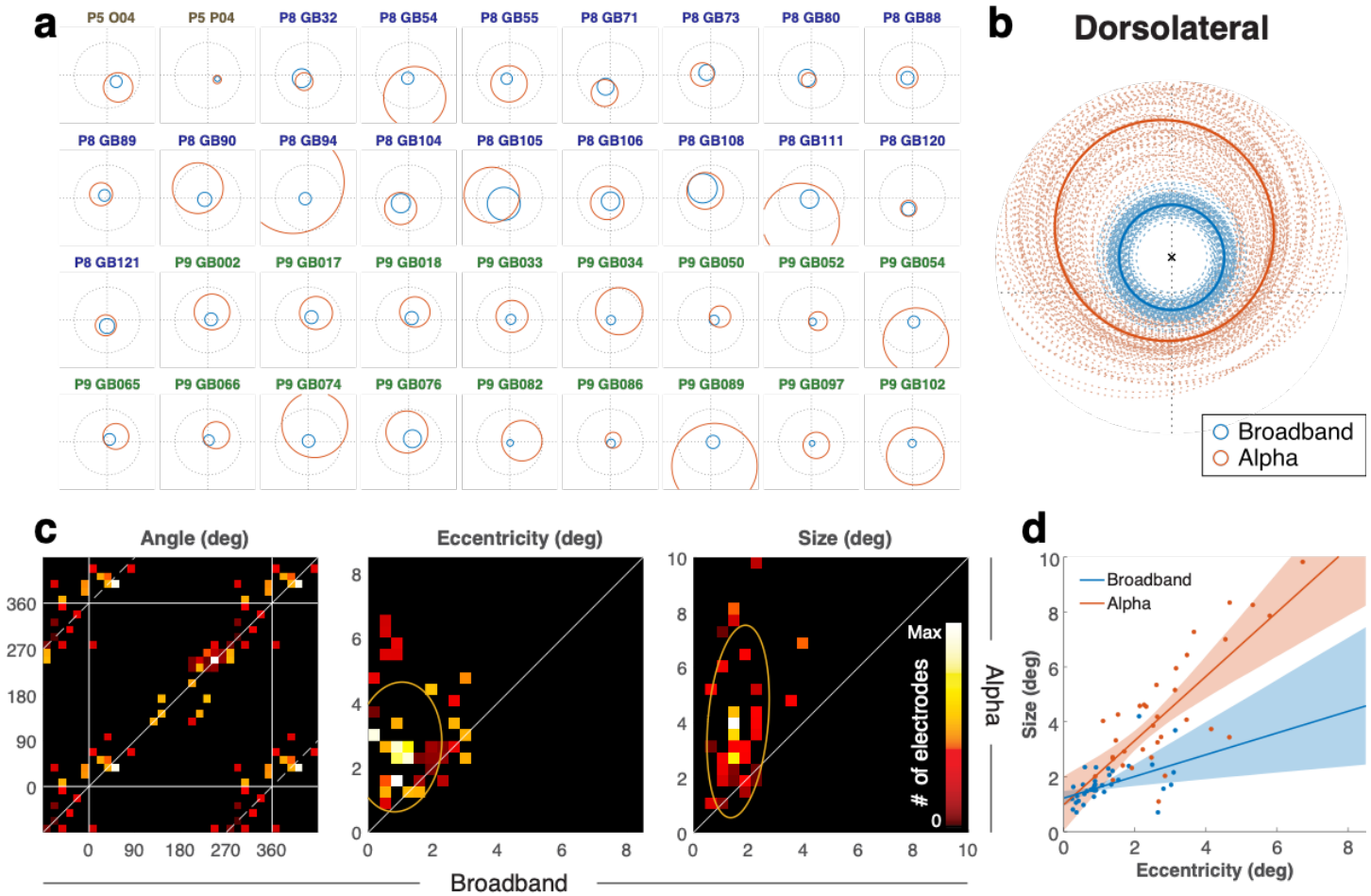

Supplementary Figure 5-1. Relations of alpha and broadband pRFs in dorsolateral. (**a**) pRF locations in dorsolateral maps. For visualization purposes, only electrodes that are more likely to be assigned to dorsolateral than to V1 to V3 are plotted, even though the probabilistic assignment included additional electrodes that are not displayed here. (**b**) pRFs were normalized by rotation (subtracting the broadband pRF polar angle from both the broadband and alpha pRF) and then scaling (dividing the eccentricity and size of both pRFs by the broadband pRF eccentricity). This puts the broadband pRF center at (0,1) for all electrodes, indicated by an 'x'. Within this normalized space, the average pRF across electrodes was computed 5,000 times (bootstrapping across electrodes). 100 of these averages are plotted as dotted lines, and the average across all 5,000 bootstraps is plotted as a solid line. (**c**) Each panel shows the relation between broadband and alpha pRF parameters in 2-D histograms. 53 electrodes were randomly sampled with replacement 5,000 times (bootstrapping), and each time they were selected they were probabilistically assigned to a visual area. The colormap indicates the frequency of pRFs in that bin (see *Comparison of alpha and broadband pRFs* in Methods 4.7). Note that the phases in the horizontal and vertical axes are wrapped to show their circular relations. The middle and right panels show the relation of eccentricity and pRF sizes, respectively. Yellow ellipses indicate the 1-sd covariance ellipses. (**d**) The plot shows pRF size vs eccentricity, both for broadband (blue) and alpha (red). As in panel **c**, the 53 electrodes were bootstrapped 5,000 times. The regression lines are the average across bootstraps, and the shaded regions are the 16th to 84th percentile evaluated at each eccentricity. Only electrodes that are more likely to be assigned to V1–V3 are plotted. See *makeFigure5_5S1.m*.

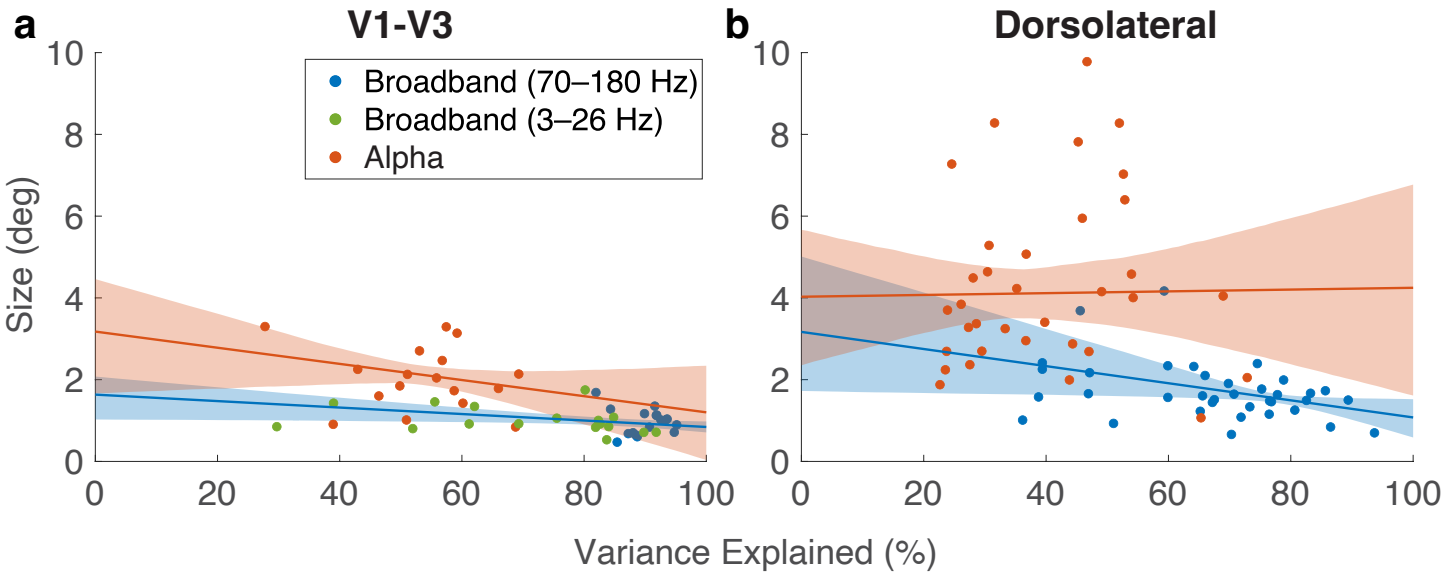

Supplementary Figure 5-2. Estimated pRF size versus cross-validated variance explained. (a) The plot illustrates the relationship between pRF size and variance explained by the pRF model for V1 to V3 maps. The red dots are for the alpha pRF model, and the red line is the best fit regression line. Broadband pRF models are shown by blue dots (high frequency broadband) and green dots (low frequency broadband). The blue regression line was fit to the combination of high and low frequency broadband. The plot shows that pRF size is larger for alpha than for broadband, irrespective of variance explained. Had the larger pRFs in the alpha model been due to greater noise, than a single regression line would fit all the data points. Error shading represents the 16th to 84th percentiles derived from 5,000 bootstrapping iterations. **(b)** Same as A except for dorsolateral maps. Here, low frequency broadband models are not included because there was little low frequency broadband signal in these electrodes. See *makeFigure5S2.m*

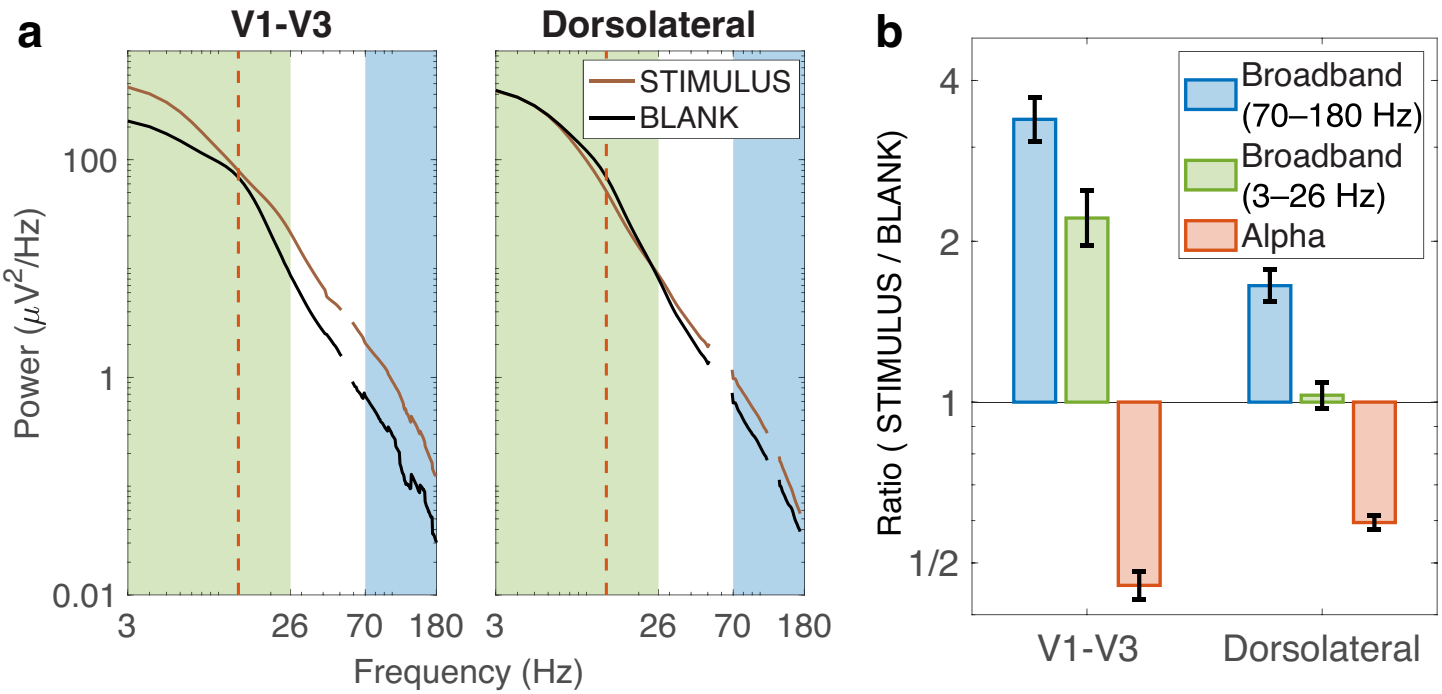

Supplementary Figure 6-1. Power in the broadband response and alpha oscillation. Each panel shows the spectral power changes averaged across all electrodes between BLANK and in-pRF stimulation (STIMULUS) conditions in V1–V3 and dorsolateral. **(a)** PSD for in-pRF (brown line) is higher than for BLANK (black line) and across all frequencies including not only high frequencies (blue region) but also low frequencies (green region) in V1–V3. In dorsolateral, on the other hand, PSD for in-pRF is higher than for BLANK only in high frequencies. Gaussian bumps at peak alpha frequencies (red dashed lines) are observed only in BLANK condition. **(b)** The ratio of PSDs between in-pRF and BLANK is positive in high-frequency broadband and negative at alpha frequency consistently in V1–V3 and dorsolateral. The ratio in low-frequency broadband is also positive in V1–V3 but is almost zero in dorsolateral. See *makeFigure6S1.m*.

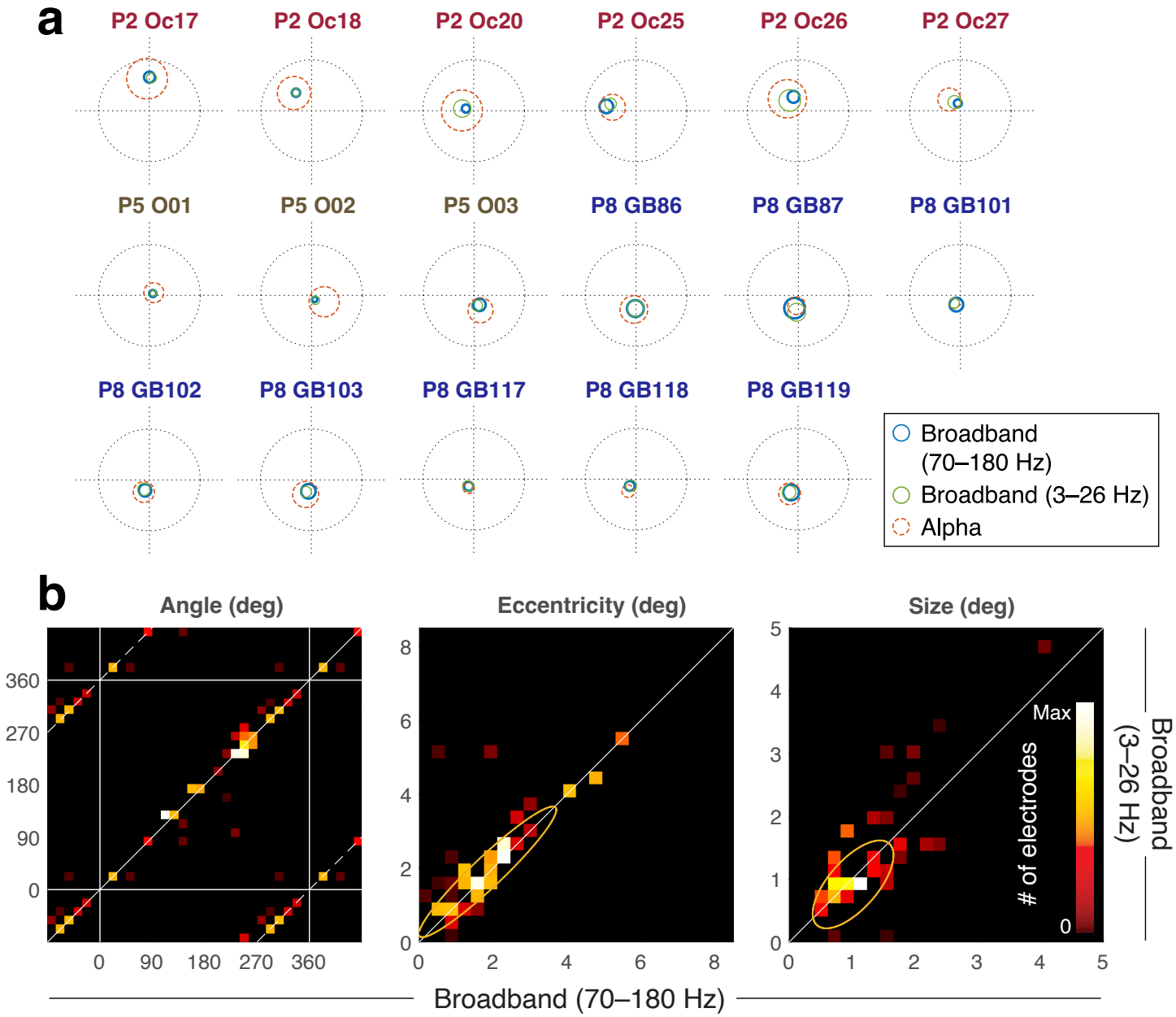

Supplementary Figure 6-2. Low broadband model comparisons. (a) PRFs for low frequency broadband (3-26 Hz) and high frequency broadband (70–180 Hz) in V1–V3 electrodes. Plotted as in Figure 5A. **(b)** PRF parameters are highly correlated between the high-frequency broadband estimates (x-axis) and the low-frequency broadband estimates (y-axis) in V1–V3. Yellow ellipses indicate the 1-sd covariance ellipses. See *makeFigure6_6S2.m*.

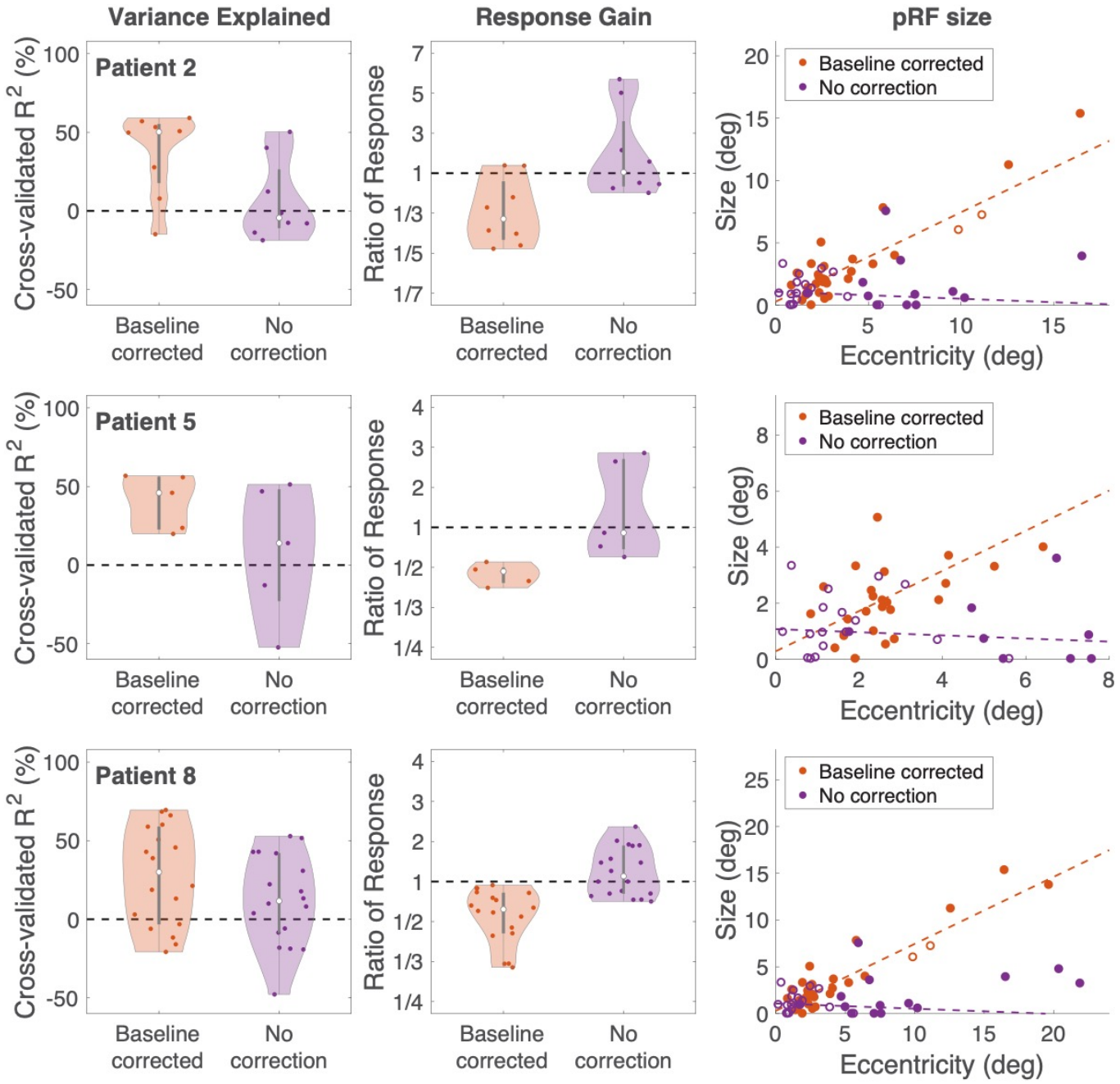

Supplementary Figure 7-1. A comparison of alpha pRFs with and without baseline correction in individual patients. We compared alpha pRF solutions that were baseline corrected (using our spectral model) or not baseline corrected (computing power within the alpha band). Each row is a separate participant. **Left**: Variance explained. The white dots are the median and the gray bars are the interquartile range. Each colored dot is one electrode and the shaded regions are smoothed histograms. **Middle**: Response gain, plotted in the same manner as variance explained. Gain is quantified as the maximum or minimum value in the pRF fitted time series (maximal for electrodes with positive gain, minimal for electrodes with negative gain). A value above 1 means that the response increased relative to baseline (positive gain). A value below 1 means the response decreased (negative gain). The baseline correction resulted in the expected negative gain. **Right**: pRF size vs eccentricity. Electrodes are colored by the sign of the gain (filled for negative, open for positive gain). The baseline corrected data shows the expected pattern of increasing pRF size with eccentricity. See *makeFigure7_7S1.m*.

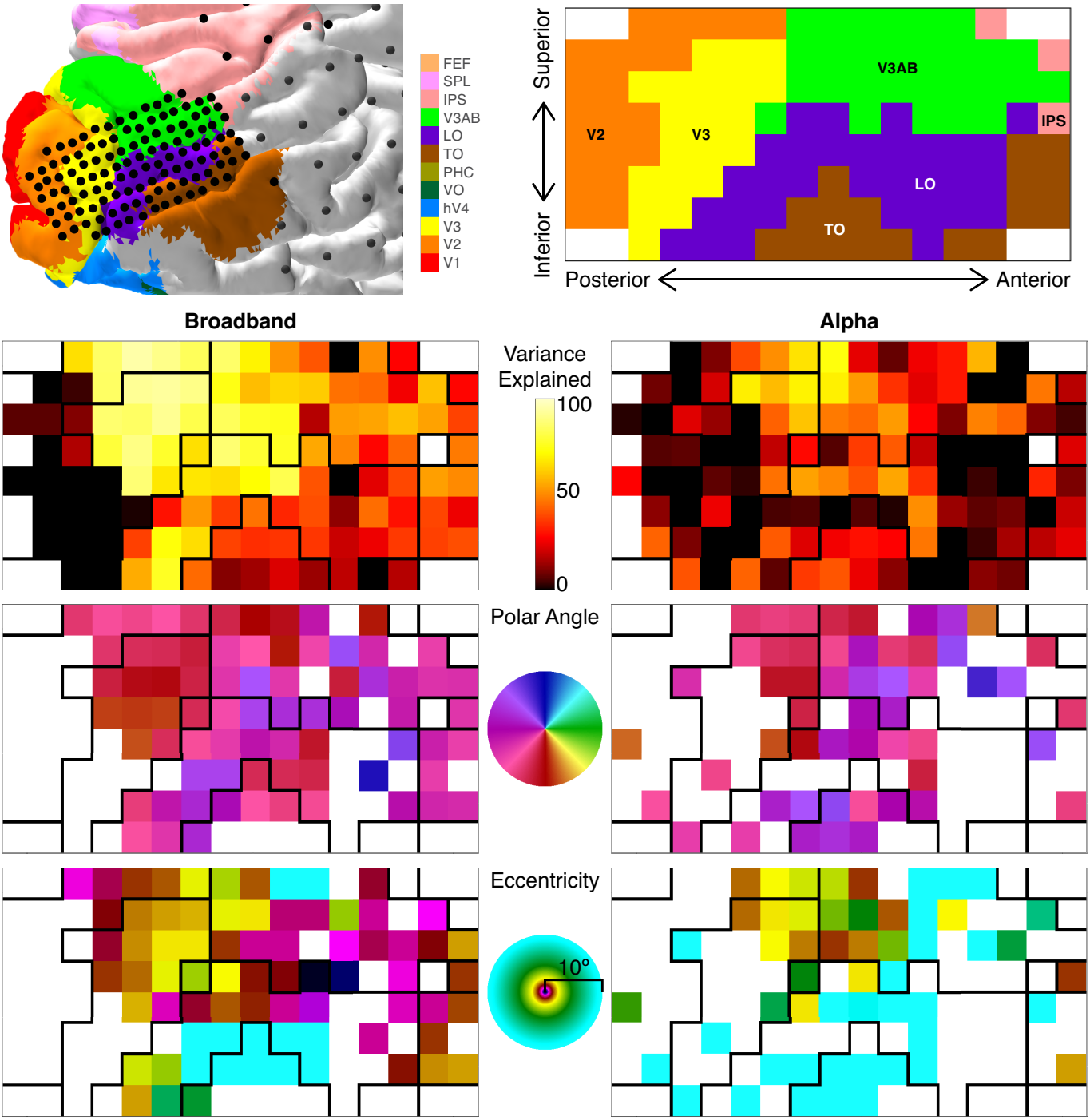

Supplementary Figure 8-1. PRF parameters from high-density grid in Patient 8. (Upper left) The electrode locations and visual areas on the brain surface from Patient 8. **(Upper right)** The visual area assignments of electrodes from the high-density grid. White spaces indicate absence of electrodes. **(Second row)** Two-fold cross-validated variance explained in pRF fitting for broadband and alpha across electrodes in the high-density grid. Electrode locations which were excluded in the preprocessing are shown as white. **(Third and Fourth rows)** Polar angles and eccentricities of estimated pRFs. Electrodes which had low variance explained (under 31% and 22% for broadband and alpha, respectively) are shown as white. See *makeFigure8S1_8S2.m*.

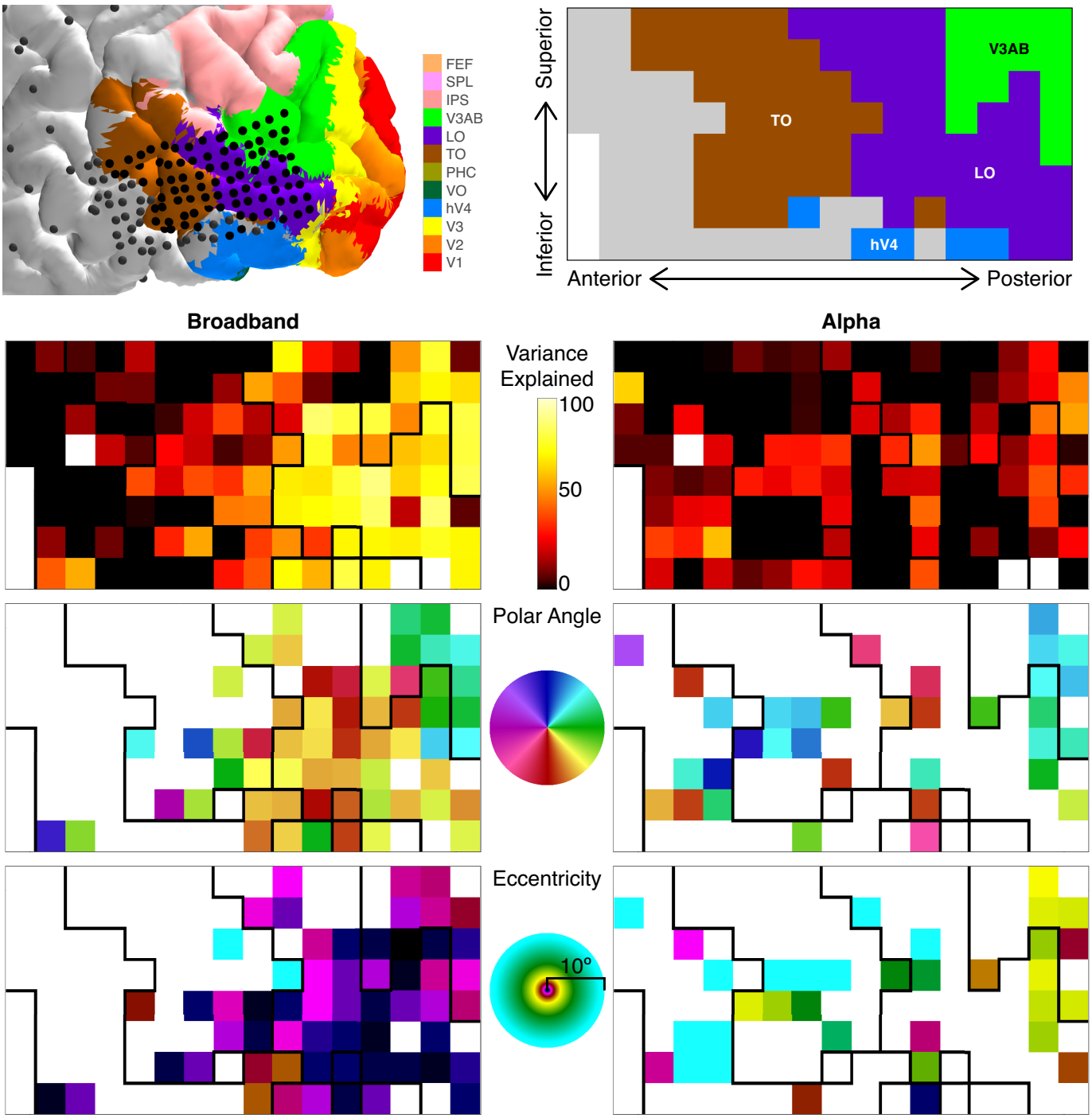

Supplementary Figure 8-2. PRF parameters from high-density grid in Patient 9. (Upper left) The electrode locations and visual areas on the brain surface from Patient 9. **(Upper right)** The visual area assignments of electrodes from the high-density grid. White spaces indicate absence of electrodes. Gray spaces indicate electrodes which were not assigned to any visual areas. **(Second row)** Two-fold cross-validated variance explained in pRF fitting for broadband and alpha across electrodes in the high-density grid. Electrode locations which were excluded in the preprocessing are shown as white. **(Third and Fourth rows)** Polar angles and eccentricities of estimated pRFs. Electrodes which had low variance explained (under 31% and 22% for broadband and alpha, respectively) are shown as white. See *makeFigure8S1_8S2.m*.

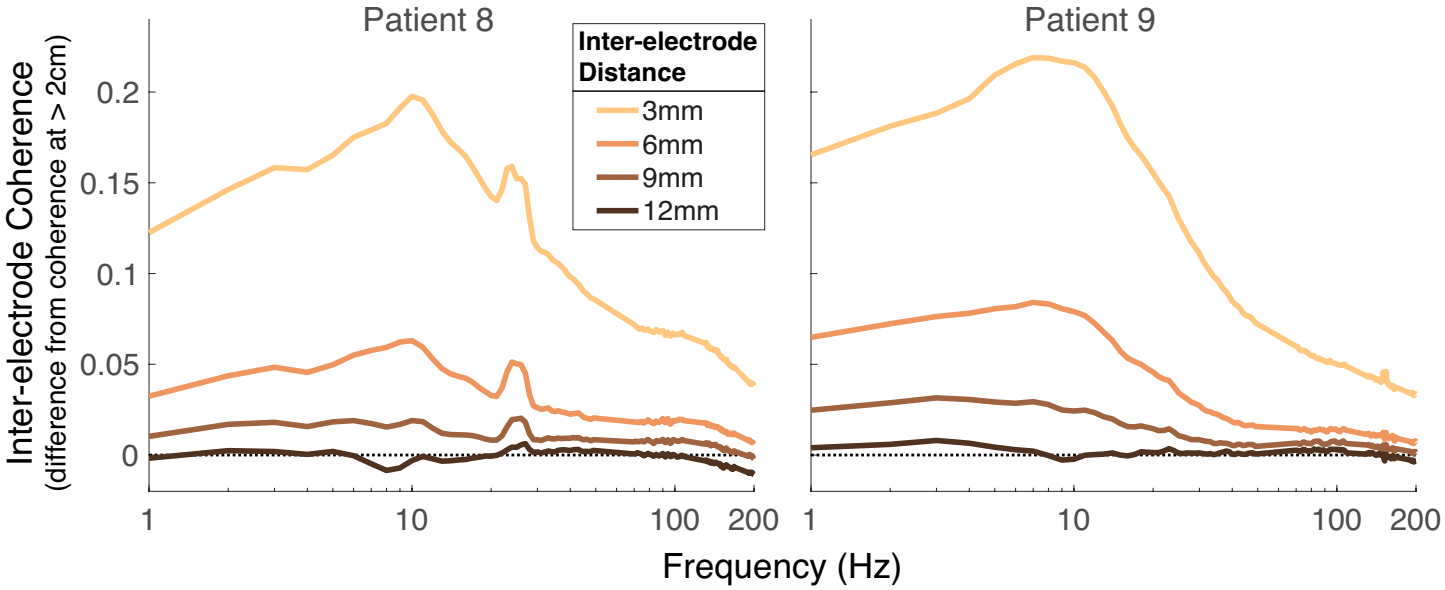

Supplementary Figure 8-3. Inter-electrode coherence in the high-density grids across 1–200 Hz. Each curve indicates the coherence averaged across electrode-pairs, binned by inter-electrode distance. The coherence for electrode pairs more than 2 cm apart was used as a baseline, and subtracted from each curve. For both patients, the coherence is highest around 10 Hz, the frequency of the alpha oscillation. See *makeFigure8S3.m*.

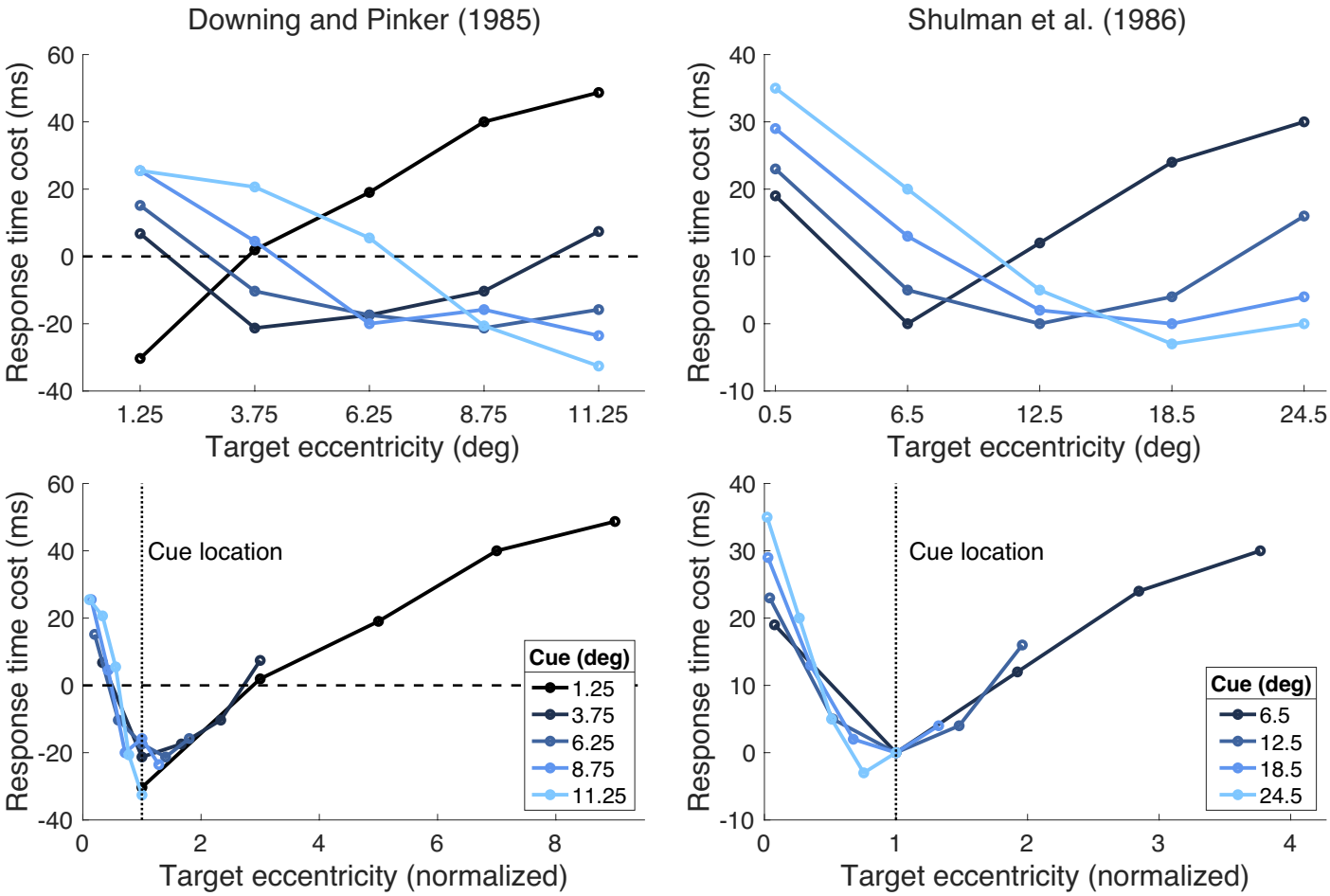

Supplementary Figure 10-1. Response time costs in previous spatial attention experiments. Left panels represent response time changes induced by endogenous attention from Downing and Pinker (1985), relative to the response time without any attentional cue. Right panels represent response time changes induced by exogenous attention from Shulman et al. (1986), relative to the response time when targets appeared at the attended locations. Lower panels are the same results as top panels after normalizing target eccentricities by dividing by the cue eccentricities. Results from the Shulman et al. paper with foveal cue locations at 0.5 degree eccentricity were excluded from the plot because after normalizing, the data from this condition has no overlap with the other conditions. See *makeFigure10S1.m*.

Graphical and statistical support for primary claims.

Here we note which analyses support each major claim in the paper and, where appropriate, how we dealt with nesting (the grouping of electrodes to individual participant).

1. *Claim: Alpha responses are accurately predicted by a pRF model (Section 2.3).*

   Support:
   - Figure 4 (left side) shows that for V1 to V3, there is greater variance explained in the alpha responses by the pRF model for visually responsive than for visually non-responsive electrodes (where "visually responsive" is defined by variance explained by the broadband pRF fits). The difference in variance explained (visually responsive vs non-responsive) is many times larger than the variability, making formal null hypothesis testing superfluous.
   - Supplementary Figure 4-2 (left) shows the same pattern for dorsolateral maps.

   Nesting:
   - Figure 4 (right side) shows that for V1–V3, the pattern observed when pooling across all electrodes is not due to the influence of a single participant's electrodes; the same pattern is observed in individual participants.
   - Supplementary Figure 4-2 (right) shows that for dorsolateral electrodes, the pattern for non-visually responsive electrodes is the same in all patients: little to no variance explained by the pRF model. There were only two patients with large numbers of visually responsive electrodes in dorsolateral maps, and in each of these patients the pattern was the same (high variance explained by the alpha pRF model).

2. *Claim: Alpha pRFs are larger than broadband pRFs (Section 2.4).*

   Support:
   - Figure 5a shows the alpha and broadband pRFs for each electrode in V1 to V3 (for electrodes whose probabilistic location is higher for V1 to V3 than for other maps). The alpha pRF is larger in nearly every case (15 out of 17). If we include all electrodes that have non-zero probability of localization in V1 to V3, the pattern is the same (33 out of 35 electrodes have larger size for alpha than for broadband).
   - Supplementary Figure 5-1a shows the same pattern for dorsolateral electrodes (electrodes whose maximum probability is in one of the dorsolateral maps): 34 of 36 electrodes have larger size for alpha than broadband pRFs. If we count all electrodes that have none-zero probability of localization in dorsolateral maps, the numbers are 41 of 45 electrodes.
   - Figure 5d (V1 to V3) and Supplementary Figure 5-1d (dorsolateral) plot pRF size vs eccentricity separately for broadband and alpha pRFs. Both of these plots show non-overlapping 68% confidence intervals for broadband vs alpha.
   - Figure 5c (V1 to V3) and Supplementary Figure 5-1c (dorsolateral) plot 2D histograms of pRF parameters, alpha vs broadband. The rightmost panel in both plots compares pRF size for alpha vs broadband. Nearly all the values are above the identity line, meaning larger size for alpha pRFs.

   Nesting:
   - In Figure 5a and Supplementary Figure 5-1a, showing alpha and broadband pRF solutions for every individual electrode, we grouped and color-coded electrodes by individual patient. The larger size for the alpha pRFs is evident in each individual patient.

3. *Claim: The alpha and broadband pRFs have similar locations (Section 2.4).*

   Support:
   - Figure 5a shows the pRF solutions for broadband and alpha in each electrode (n=17). The broadband pRFs have similar centers and are nearly always inside the alpha pRFs. We report in the text that on average, 92.3% of the broadband pRFs (up to 1-SD) are inside the alpha pRFs (up to 1-SD). To show that this is not a trivial consequence of the alpha pRFs being larger, we recomputed

this value after shuffling the electrodes, and the number decreases to 30.0%. We do not think a null hypothesis statistical test is needed to show that these percentages are different.

- The same visualization (Supplementary Figure 5-1a) shows that in dorsolateral maps, the broadband pRFs are inside the alpha pRFs. The calculation shows that the containment percentage is 98.0%, decreasing to 25.7% with a shuffle analysis, again a large effect well above the noise.
- The similarity in pRF polar angle is shown in a 2D histogram in Figure 5c (left panel) for V1 to V3. Nearly all the data are concentrated close to the identity line.
- The same pattern is shown for the dorsolateral maps in Supplementary Figure 5-1c.

Nesting:

- The similarity in pRF location between broadband and alpha is observed across individual patients, shown in Figure 5a and Supplementary Figure 5-1a (grouped and color coded by patient).

4. *Claim: The difference in pRF size is not due to a difference in temporal frequency between broadband and alpha. (Section 2.5)*

Support:

- Figure 6 shows the distributions of broadband pRF sizes, separated into high frequency broadband (70–180 Hz) and low-frequency broadband (3–26 Hz), compared to alpha pRF sizes. The alpha pRF size is more than double those of low- and high-frequency broadband, whereas the low and high frequency broadband pRF sizes are the same as each other.
- Supplementary Figure 6-2b shows 2D histograms of pRF parameters in V1 to V3, comparing low- and high-frequency broadband. The angle, eccentricity, and size histograms all show the majority of the data lying on or near the identity line, confirming that low- and high-frequency broadband pRFs are similar, including the size. This differs from the comparison between high frequency broadband and alpha, in which the pRF sizes differ (see Claim 2 above).

Nesting:

- Supplementary Figure 6-2a shows that pRF sizes for high- and low-frequency broadband for each individual electrode. Electrodes are grouped and color-coded by individual patient. Each patient shows a similar size for low- and high-frequency broadband pRFs.

5. *Claim: The accuracy of the alpha pRFs depends on the model-based calculation. (Section 2.6)*

Support:

- Figure 7 compares pRF solutions with and without the model-based baseline correction.
    - Left panel: The figure shows a higher cross-validated variance explained for the model-based method (43% vs 10%, median).
    - Middle panel: The model-based method also shows a consistently negative gain (29 out of 31 electrodes), whereas without correction there is a mixture of positive and negative gain (14 negative, 17 positive), inconsistent with 100 years of measurements of the alpha oscillation.
    - Right panel: The estimated pRF size correlates positively with eccentricity when doing the baseline correction, but not without the correction

Nesting:

- All three patterns described above are evident in individual patents (Supplementary Figure 7-1).

6. *Claim: Alpha oscillations are coherent across a larger spatial extent than broadband signals. (Section 2.7)*

Support:

- Figure 8 (bootstrapping shows significant differences between broadband and alpha coherence)

Nesting:

- The results are not averaged but are provided for individual patients